

**MODELING OF LIFE LIMITING PHENOMENA IN THE
DISCHARGE CHAMBER OF AN ELECTRON BOMBARDMENT
ION THRUSTER**

**PREPARED FOR
MARSHALL SPACE FLIGHT CENTER
NATIONAL AERONAUTICS AND SPACE ADMINISTRATION
GRANT NAG 8-020**

FINAL REPORT

FEBRUARY 1991

ARVIND K. HANDOO

AND

PRADOSH K. RAY

MECHANICAL ENGINEERING DEPARTMENT

TUSKEGEE UNIVERSITY

TUSKEGEE, ALABAMA 36088

(NASA-CR-190045) MODELING OF LIFE LIMITING
PHENOMENA IN THE DISCHARGE CHAMBER OF AN
ELECTRON BOMBARDMENT ION THRUSTER Final
Report (Tuskegee Inst.) 99-0 CSCL 21C

N92-21176

Unclass
0073958

63/20

ABSTRACT

An experimental facility to investigate the low-energy sputtering of metal surfaces with ions produced by an ion gun is described. The energy of the ions ranged from 10 to 500 eV. Cesium ions with energies from 100 to 500 eV were used initially to characterize the operation of the ion gun. Subsequently, argon and xenon ions were used to measure the sputtering yields of cobalt, cadmium and chromium at an operating pressure of 2×10^{-5} Torr. The ion current ranged from 0.0135 μA at 10 eV to 0.84 μA at 500 eV. The targets were electroplated on a copper substrate. The surface density of the electroplated material was approximately 50 $\mu\text{g}/\text{cm}^2$. The sputtered atoms were collected on an aluminium foil surrounding the target. Radioactive tracers were used to measure the sputtering yields.

The sputtering yields of chromium were found to be much higher than those of cobalt and cadmium. The yields of cobalt and cadmium were comparable, with cobalt providing the higher yields. Cobalt and cadmium targets were observed to sputter at energies as low as 10 eV for both argon and xenon ions. The chromium yields could not be measured below 20 eV for argon ions and 15 eV for xenon ions. On a linear scale the yield-energy curves near the threshold energies exhibit a concave nature. The existence of sputtering at ion

energies as low as 10 eV qualitatively explain the erosion observed at the upstream baffle and cathode pole piece of the J-series mercury ion thrusters.

TABLE OF CONTENTS

	<u>Page</u>
ABSTRACT	i
TABLE OF CONTENTS	iii
LIST OF FIGURES	v
LIST OF TABLES	vii
INTRODUCTION	1
BACKGROUND INFORMATION ON LOW-ENERGY SPUTTERING	6
Introduction	6
Low-Energy Sputtering and Threshold Energy	7
EXPERIMENTAL SET-UP AND PROCEDURE	11
Introduction	11
Measurement of the Sputtering Yield	13
Data Analysis	17
Vacuum System	21
Ion Gun	23
Target-Collector Assembly	24
Experimental Procedure	28
RESULTS AND DISCUSSION	33
Calibration of the Multichannel Analyzer	33
System Characterization	37
A. Vacuum System Operation	37
B. Ion Gun Operating Characteristics	37
C. Effect of Pressure on Sputtering by Cesium Ions	40
D. Cesium Ion Beam Characteristics	40

TABLE OF CONTENTS (Continued)

	<u>Page</u>
Sputtering Yields of Cobalt by Argon and Xenon Ions	42
A. Operating Pressure	42
B. Sputtering Yield by Argon Ions	45
C. Sputtering Yield by Xenon Ions	47
D. Sputtering Yields Near Threshold Energy	50
Sputtering Yields of Cadmium by Argon and Xenon Ions	50
A. Sputtering Yields by Argon and Xenon Ions	50
Sputtering Yields of Chromium by Argon and Xenon Ions	55
A. Sputtering Yield by Argon Ions	55
B. Sputtering Yield by Xenon Ions	58
C. Sputtering Yields Near Threshold Energy	58
Comparative Evaluation of Sputtering Yields	62
MODELING OF DISCHARGE CHAMBER COMPONENT EROSION	68
Introduction	68
Physical Sputtering	69
A. Mathematical Model	69
B. Screen Grid Centerline Erosion	72
C. Baffle Erosion	75
CONCLUSIONS	77
REFERENCES	79
APPENDIX A: SPUTTERING YIELD DATA	82
DISTRIBUTION LIST	86

LIST OF FIGURES

<u>Figure</u>	<u>Title</u>	<u>Page</u>
1	Schematic Diagram of 30-cm J-series Thruster Discharge Chamber	3
2	Simplified Decay Schemes of ^{57}Co , ^{109}Cd and ^{51}Cr	18
3	Schematic View of the Vacuum Chamber	22
4	Schematic of the Gas Flow Unit	25
5	Ion Gun	26
6	Substrate Dimensions	27
7	Schematic of the Ion Gun and the Collector Assembly	29
8	Overall Experimental Set Up	30
9	Location of the Photoelectric Peak in the Multichannel Analyzer	34
10	Gamma Ray Energy Spectra of ^{57}Co , ^{109}Cd , ^{51}Cr and a Typical Background Spectrum	35
11	Typical Pumpdown Curve for the Vacuum Chamber	38
12	Variation of the Sputtering Yield with Ion Gun-Target Distance	39
13	Effect of Pressure and Current on the Sputtering Yield of Cobalt by Cesium Ions	41
14	Sputtering Yield of Cobalt by Cesium Ions	43
15	Sputtering Yield of Cobalt by Argon Ions at Different Operating Pressures	44
16	Sputtering Yield of Cobalt by Argon Ions	46
17	Sputtering Yield Ratio of Cobalt by Argon Ions	48
18	Sputtering Yield of Cobalt by Xenon Ions	49

LIST OF FIGURES (Continued)

<u>Figure</u>	<u>Title</u>	<u>Page</u>
19	Sputtering Yield of Cobalt by Argon Ions Near Threshold Energy	51
20	Sputtering Yield of Cobalt by Xenon Ions Near Threshold Energy	52
21	Sputtering Yield of Cobalt by Argon and Xenon Ions Compared with Yield of Nickel by Argon Near Threshold Energy	53
22	Sputtering Yield of Cadmium by Argon and Xenon Ions	54
23	Sputtering Yield of Cadmium by Argon and Xenon Ions Near Threshold Energy	56
24	Sputtering Yield of Chromium by Argon Ions	57
25	Sputtering Yield of Chromium by Xenon Ions	59
26	Sputtering Yield of Chromium by Argon and Xenon Ions Near Threshold Energy	60
27	Comparison of the Yields of Cobalt, Cadmium and Chromium by Argon Ions	63
28	Comparison of the Yields of Cobalt, Cadmium and Chromium by Argon Ions Near Threshold Energy	64
29	Comparison of the Yields of Cobalt, Cadmium and Chromium by Xenon Ions	65
30	Comparison of the Yields of Cobalt, Cadmium and Chromium by Xenon Ions Near Threshold Energy	66
31	Variation of Screen Grid Centerline Erosion with Ratio of Doubly to Singly Charged Ions	74

LIST OF TABLES

<u>Table</u>	<u>Title</u>	<u>Page</u>
1	Radioisotopes and Energies of the Photoelectric Peaks Used in Calibrating the Mutichannel Analyzer	33
2	Counting Efficiency of the Photoelectric Peaks of ^{57}Co , ^{109}Cd and ^{51}Cr	36
A.1	Sputtering Yield Data of Cobalt	83
A.2	Sputtering Yield Data of Cadmium	84
A.3	Sputtering Yield Data of Chromium	85

INTRODUCTION

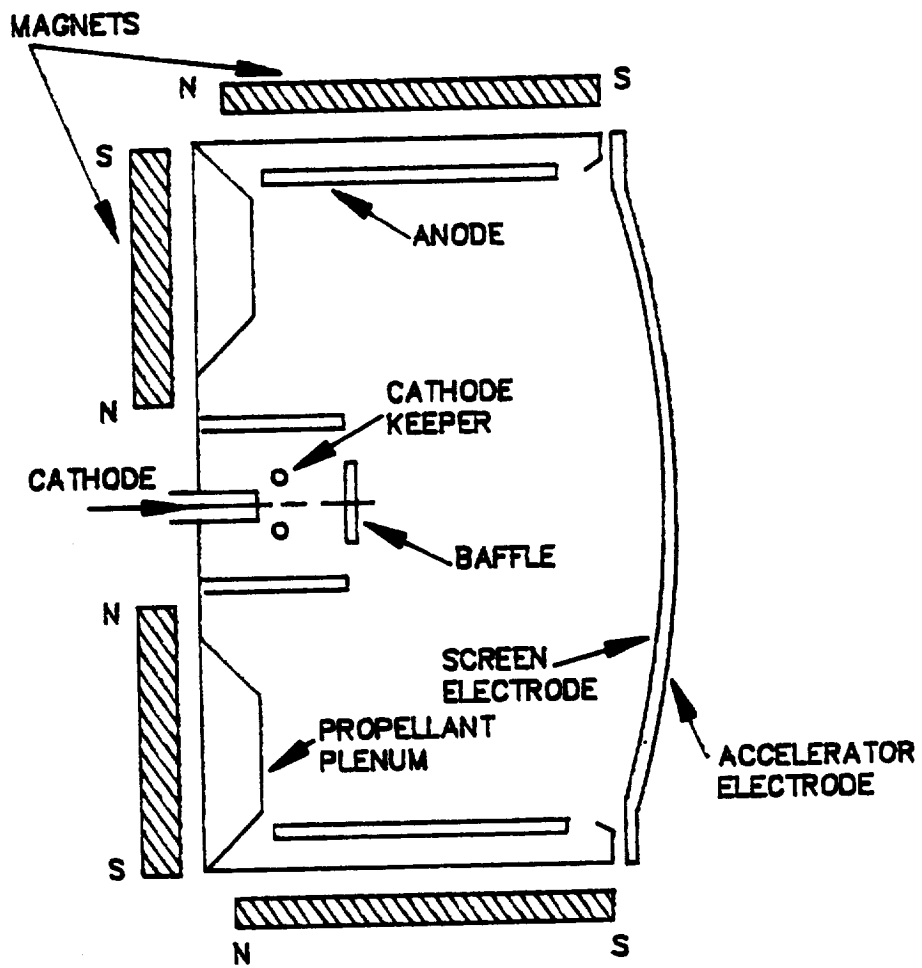
Ion engines are being considered for many future space missions to meet both the primary and the auxiliary propulsion requirements [1-4]. In these thrusters, ions of suitable vapors (mercury) or gases e.g., argon, xenon are created in a discharge chamber by electron bombardment [5,6] or radiofrequency ionization process [7,8]. In an electron bombardment thruster, a cathode serves as the source of electrons which are accelerated by an electric field established by positively biasing the discharge chamber walls. The electrons are made to spiral through the neutral propellant atoms by applying a magnetic field to improve the ionization efficiency. The positive ions are extracted and accelerated by the electric field of a multiple-aperture accelerator-screen grid system to form the ion beam. The ions are subsequently expelled from the thruster, thus providing momentum to the spacecraft. The positive ion beam is neutralized after it exits from the thruster by the addition of an equal number of electrons.

Life limiting tests, lasting nearly 10,000 hours, have been conducted on the 700-series and J-series 30-cm and 5-cm diameter electron bombardment mercury ion thrusters [9-11]. From these tests, it has been observed that the most serious life limiting phenomena is the sputtering erosion of the

discharge chamber components which come in contact with the ions. The sputtered material is re-deposited on the internal surfaces of the discharge chamber and as the coating of the sputtered material builds up in thickness, it peels away from the surface in the form of flakes which may be of sufficient size to cause electrical shorts or arcing. Recent extended testing of a J-series 30-cm diameter thruster using xenon and 15 to 35 A discharge currents also revealed significant component erosion [12]. A tantalum baffle in this thruster was observed to erode at a rate as high as 0.9 $\mu\text{m/hr}$. Even higher erosion rates were observed at higher discharge currents [13].

The discharge chamber of a 30-cm diameter J-series mercury ion engine is shown schematically in Fig. 1. The surfaces of the discharge chamber at the cathode potential are subjected to bombardment by ions contained in a plasma potential of approximately 32 V. The amount of doubly charged ions in this plasma for 2-A beam current is about 15 percent. Hence the surfaces at the cathode potential are bombarded by ions having up to 64 eV energies. Since the highest current densities occur on the chamber centerline, the highest wear rates in the main discharge chamber take place at the screen grid centerline and at the downstream baffle cover centerline.

Significant wear rates have also been observed on the cathode pole piece-baffle subassembly of the mercury ion engine and particularly, on the upstream baffle cover at the



NOT TO SCALE

Figure 1. Schematic Diagram of 30-cm J-series Thruster Discharge Chamber

centerline [11]. The baffle and pole piece erosion with subsequent deposition of material onto the cathode keeper and its supporting structure remains as the major technology issue of the J-series thruster [5]. However, the mechanism by which this erosion takes place is not understood. In the region near the cathode pole piece, the ion energies are approximately that of the cathode keeper potential of 10 V [11]. Also, there are some doubts about the formation of doubly charged ions within the confines of the cathode pole piece [14]. Hence, the surfaces around the cathode pole piece come in contact with ions having energies of the order of 10 eV. However, it has generally been assumed that a threshold energy exists for the sputtering process to occur and linearly extrapolated data obtained from various experiments indicate the threshold energies in the region of 15 to 35 eV.

In view of this, an experimental study has been initiated to investigate the low-energy ion sputtering phenomena, particularly near the threshold energy. The objective of this research is to set up an experimental assembly to bombard materials with low-energy ions and obtain sputtering yield data under well-defined experimental conditions. It should be noted though, that a recent study has revealed that the energies of ions produced near the cathode can be several times the anode-to-cathode potential difference [15]. A laboratory model ring-cusp discharge chamber using xenon was used in this investigation. At discharge currents

exceeding 10 A, a fraction of ions was found to originate near the cathode orifice region having energies as high as 50 eV. The percentage of ions having energies greater than the anode-to-cathode potential difference increased with the increase in discharge current. The number of ions at these high energies may be large enough to produce the observed erosion rates at the upstream baffle even in discharge chambers using currents of the order of 10 A.

BACKGROUND INFORMATION ON LOW-ENERGY SPUTTERING

Introduction

When a surface is subjected to bombardment by ions of sufficient kinetic energy, the collision processes may provide enough energy to individual atoms of the target to escape from the surface. This process of ejection of atoms from a surface is called sputtering. The total erosion in sputtering is quantified by a useful parameter known as the sputtering yield, S , which is defined as the average number of atoms removed from the surface per incident ion, i.e.,

$$S = \frac{\text{Number of sputtered atoms}}{\text{Number of incident ions}} \quad (1)$$

Sputtering yields as a function of ion energy have been measured for a variety of target-ion combinations. The yields depend on the type of ion, its energy and angle of incidence, and on the nature and surface binding energies of the target. From the extrapolated yield values at the low energy end it has been generally accepted that below a threshold ion energy, which is about 15 to 35 eV, no sputtering should take place. However, in this ion energy range the sputtering yield is so small that it may be difficult to

determine it experimentally even in long sputtering runs. Hence there has always been some doubt on the existence of a threshold energy for sputtering.

Low-Energy Sputtering and Threshold Energy

Sputtering thresholds have been the subject of numerous experimental investigations during the 1950s and 1960s. The most extensive and systematic experiments in this area were performed by Wehner and his colleagues. In all of these investigations, the targets were immersed like a negative Langmuir probe in a low-pressure mercury or noble gas plasma maintained between a separate independent cathode and an anode. The high density of the plasma was achieved by using magnetic and in some cases, both magnetic and geometric compressions. Despite these studies, disagreements exist among the published values of the threshold energy for various ion-atom combinations.

The investigation of sputtering at low ion energies has always been associated with great experimental difficulties. The problem consists of determining the minimum ion energy E_0 which the bombarding ions must have to be able to dislodge target atoms as well as the measurement of the sputtering yields as a function of ion energy E , where E is slightly greater than E_0 .

The sputtering yields of nickel and cobalt near the threshold region using mercury and argon ions were measured by Morgulis and Tischenko [16]. In these studies the yields

were determined by using radioactive tracer atoms and sputtering yields down to 10^{-4} atom/ion were measured. At very low ion energies, the yield-energy curves were found to have a concave character and threshold energies were determined by linear extrapolation. Sputtering thresholds were found to be 7 to 8 eV for nickel and cobalt with both mercury and argon ions.

The sputtering yields of 26 metals under normally incident mercury ion bombardment in the energy range of 30 to 400 eV were measured by Wehner using ion current densities up to 15 mA/cm² [17]. In this investigation, yields were obtained by measuring the weight loss from the target. Subsequently, Wehner and his colleagues reported sputtering yields of 28 elements for argon and neon ions with energies from 50 to 600 eV [18] and of 30 elements for helium, krypton and xenon ions with energies from 100 to 600 eV [19]. In these studies, 6-mm diameter spheres of various elements were used as targets. The plasma was created by maintaining a current of several amperes between a thermionic oxide cathode and an anode. The ion current densities were as high as 15 mA/cm². The weight loss method was also used in these studies to determine the sputtering yields. However, the weight loss method is not sensitive enough to provide sputtering yields at low ion energies. Since yields much below 0.1 atom/ion cannot be measured by this method threshold energies were not determined in these studies.

The widest range of data covering many materials has

been collected using spectroscopic method by Stuart and Wehner [20]. Sputtering yields as low as 10^{-5} atom/ion have been obtained for several elements by using this method. The sputtering yield data below the 50 eV region were found to have steep slopes on semi-logarithmic plots. Wehner and Anderson extrapolated these curves to an infinite slope and in this way defined a threshold energy for sputtering. The estimated threshold energies ranged from 12 to 35 eV [21]. These values are approximately 4 times the surface binding energies of the target atoms. The masses of the ion and the target atom were found to have no correlation with the threshold energy.

Askerov and Sena obtained the sputtering yield data of 14 metals by mercury ions with current densities of 300 to 500 mA/cm² and with ion energies from 20 to 200 eV [22]. The high current density was achieved by using both magnetic and geometric compressions. The yields were determined by measuring the decrease in plasma light intensity which passed through the sputtered material deposited on a glass wall. The cube root of the sputtering yield was found to vary linearly with the ion energy. Threshold energies were estimated by extrapolation and ranged from 4 eV for gold to 35 eV for tantalum.

A general disadvantage of the plasma discharge systems is that the irradiation conditions are somewhat poorly defined and impurities in the plasma could contribute to the

measured yields. Moreover, at ion energies near the threshold, different charge states of the ions could provide erroneous values of the sputtering yield.

An excellent summary of even earlier work on measurement of sputtering thresholds has been provided by Stuart and Wehner in Reference 20.

EXPERIMENTAL SET-UP AND PROCEDURE

Introduction

Since all of the sputtering yield measurements done earlier used a low-pressure, high-density plasma created in a vacuum arc, we decided to use an ion gun for these experiments. In an ion gun, a stream of ions, generated from some source, is accelerated to a desired energy by passing the ions through a series of electric fields maintained between electrodes. The experimental system is designed in such a way that the bombarding ions are focused to a fine spot on the target surface with a well-defined energy.

Space-charge in the ion beam represents the fundamental limit on the maximum current density. Child's law indicates that the ion current density, J^+ , which can be drawn across a plane gap by a given potential difference, V , is proportional to $V^{1.5}$. Thus the fundamental disadvantage of ion guns is that the ion beams are limited to low current densities. Moreover, the lower the kinetic energy of the beam, the lower is the maximum current density that can be generated. However, ion guns have the advantage of producing a monoenergetic beam with a low energy spread down to very low ion energies.

The ion current density at the target is generally considered to be an important parameter in any experiment

involving sputtering yield measurement. A target surface is always covered with some adsorbed layers of gas to which it is exposed. Hence, before any sputtering is undertaken for quantitative measurements, the surface should be made as free of adsorbed layers of gases as possible. In low energy sputtering experiments using an ion gun, it is desirable to operate the vacuum chamber at as low a pressure as possible. However, maintaining an ultra high vacuum (of the order of 10^{-9} Torr or less) involves a complex pumping system and a time consuming baking process each time the vacuum chamber is opened. Also, at such a low operating pressure, the ion current obtained at low energies becomes too small to be useful in sputtering process. In a trade-off, we decided to run our experiments in the 10^{-5} to 10^{-6} Torr pressure range (mainly at 10^{-5} Torr for the noble gases), even though some reduction of sputtering was expected due to adsorption of ambient gases on the target surface.

The nature of gas adsorption in studies of ion-surface interactions can be illustrated by noting that with an incident ion current density of 0.1 mA/cm^2 , the ion impact rate at the surface is $6.3 \times 10^{14} \text{ ions/cm}^2\text{-sec}$. Since, surfaces generally have atom densities of about $2 \times 10^{15} \text{ per cm}^2$, at 0.1 mA/cm^2 , the ions impact each surface atom approximately 20 times per minute. The flux of atoms or molecules, Z , of the ambient gas arriving at the target surface is [23]

$$Z = \frac{3.5 \times 10^{22} P}{\sqrt{MT}} \quad (2)$$

where

P = the pressure of the ambient gas in Torr

M = the molecular weight of the ambient gas

T = the temperature of the ambient gas in °K

At an operating pressure of 1×10^{-5} Torr, the noble gas atoms will strike the surface approximately 80 times during the same period. However, the partial pressures of the residual gas molecules is generally much lower (about 1×10^{-7} Torr in our experiments due to the extensive pumpdown of the vacuum chamber before the introduction of the operating gases). Thus the residual gas molecules will impinge about 1 time on the surface atom per minute. Since the sticking coefficients of noble gas atoms are substantially smaller than 1 on most surfaces, it can be seen that the target surface under an ion bombardment of 0.1 mA/cm^2 at an operating pressure of 1×10^{-5} Torr will have a small amount of adsorbed gases which is expected to inhibit the sputtering process to some extent.

Measurement of the Sputtering Yield

The total number of sputtered atoms is proportional to the ion current, the sputtering yield and the exposure time of the target. To obtain a sufficient amount of sputtered atoms at a given ion energy and in a reasonable exposure time, the ion current should be as high as possible. At

lower ion energies where the value of the sputtering yield is small, the exposure time is accordingly increased to obtain a measurable amount of the sputtered atoms.

Several methods have been tried successfully to measure the sputtering yields at very low ion energies. The direct method is to measure the weight loss of the target after each run but this requires the use of an ion beam of very high current density [17-19]. Morgulis and Tischenko used a radioactive tracer technique where a certain amount of a radioisotope is mixed with the target material [16]. As sputtering targets, they used an alloy of nickel with 1% radioactive ^{60}Co for one set of runs and pure nickel, electrolytically coated with a layer of ^{60}Co for another set of runs.

Sputtering yields have also been obtained by measuring the decrease in plasma light intensity which pass through the sputtered material deposited on a glass wall surrounding the target [22,24]. Obviously, this method also requires the use of very high ion current densities so that a significant amount of sputtered material is deposited on the glass tube to reduce the plasma light intensity sufficiently.

Stuart and Wehner used the spectroscopic method to measure the sputtering yields down to a very low ion energy. The sputtered atoms, which are mostly neutral, are elevated to an excited state in the plasma. These excited atoms generate characteristic spectral emission lines which are superimposed on the emission spectrum of the discharge gas.

The intensity of the emission spectrum of the sputtered atoms is assumed to be proportional to the sputtering yield. The yield was measured in arbitrary units as a function of ion energy. The absolute yields were determined by fitting the yield curve in arbitrary units to the absolute values, obtained in the conventional way by measuring the weight loss of the target.

Since the ion current densities in our experiments are expected to be two orders of magnitude lower than the ion current densities used by others using plasma discharge, the total amount of sputtered material is expected to be very small even after a prolonged exposure. Of all the methods used in measuring the sputtering yield, the radioactive tracer method and the spectroscopic method appear to be the most sensitive ones when the amount of the sputtered material is very small. The spectroscopic method is not applicable to our measurements. Hence we decided to use the radioactive tracer method in our experiments. When the target, mixed with a suitable radioactive isotope, is bombarded by ions, some of the radioactive atoms are sputtered along with the nonradioactive atoms of the target and are deposited on a collector. The amount of radioactive atoms in the sputtered material is then a measure of the total sputtering yield.

The disadvantage of the radioactive tracer method is that few suitable radioisotopes are available which can be used as radioactive tracers to enable one to measure the

sputtering yield. The criteria for selecting a radioactive tracer for sputtering yield measurement are:

- (1) the element can be electroplated on a metal substrate
- (2) the radioisotope should have relatively long half-life, of the order of 20 days or more, so that a complete set of data can be acquired before the target becomes too weak to be useful, and
- (3) the radioisotope decays by emitting gamma rays of relatively low energy, of the order of 500 KeV or less, so that the shielding and safety problems associated with handling the radioactive target are minimized.

Cobalt was chosen as the target material initially because the radioactive isotope, ^{57}Co , has long half-life and emits low-energy gamma rays. The half-life of ^{57}Co is 270 days and it decays predominantly by emitting gamma rays with 122 keV energy. Cadmium was chosen as the next target material as one of its isotopes, ^{109}Cd , also has a long half-life of 453 days. The gamma rays emitted by ^{109}Cd have 88 keV energy. After acquiring the experience of handling these radioactive targets, we decided to try an electroplated chromium target. The radioactive isotope of chromium, ^{51}Cr , has a short half-life of 27.7 days and 9.85 percent of the atoms decay by emitting gamma rays with 320 keV energy. Whereas the total amount of activity of the cobalt and cadmium targets were 600 μCi each (0.1% ^{57}Co and 0.3% ^{109}Cd), that of the chromium target was 57.6 μCi (0.001% ^{51}Cr). Simplified decay schemes of ^{57}Co , ^{109}Cd and ^{51}Cr are shown

in Fig. 2..

The gamma rays emitted by the radioactive tracer atoms were counted by a 75 mm x 75 mm NaI (Tl) scintillation crystal having a 16-mm diameter, 57-mm deep well. The gamma rays deposited their energy in the scintillation crystal either through photoelectric interaction or Compton scattering process. The scintillation crystal was connected to a 1024-channel analyzer which recorded the energies that the individual gamma rays deposited in the crystal. For monoenergetic gamma rays, the multichannel analyzer produced a photoelectric peak and a Compton scattering continuum. The analyzer was set such that only the photoelectric peak was counted. Standard gamma ray sources with known disintegration rates were used to determine the efficiencies of counting the gamma rays under the photoelectric peak.

Data Analysis

Let N be the number of atoms disintegrating per unit time from a standard gamma ray source. Let N' be the total number of gamma rays counted under the photoelectric peak from the standard source over a time period t . Then the efficiency of counting gamma rays under the photoelectric peak, η , is given by

$$\eta = \frac{N'}{Nt} \quad (3)$$

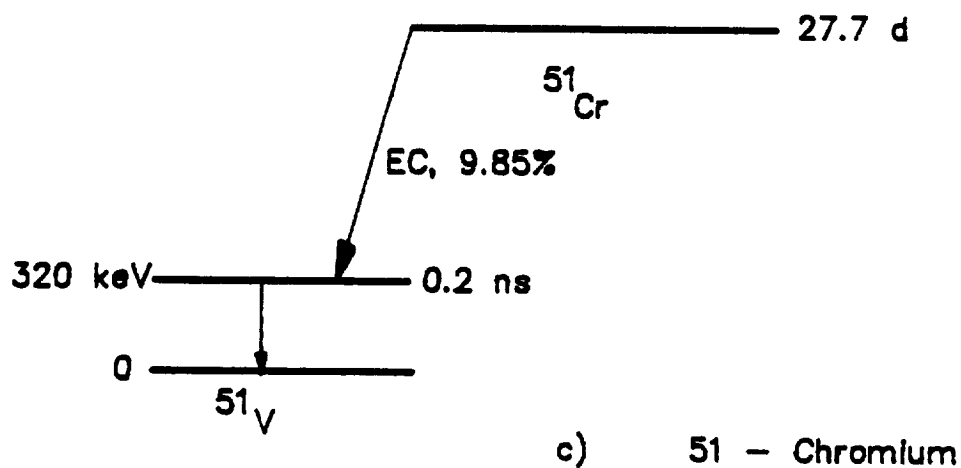
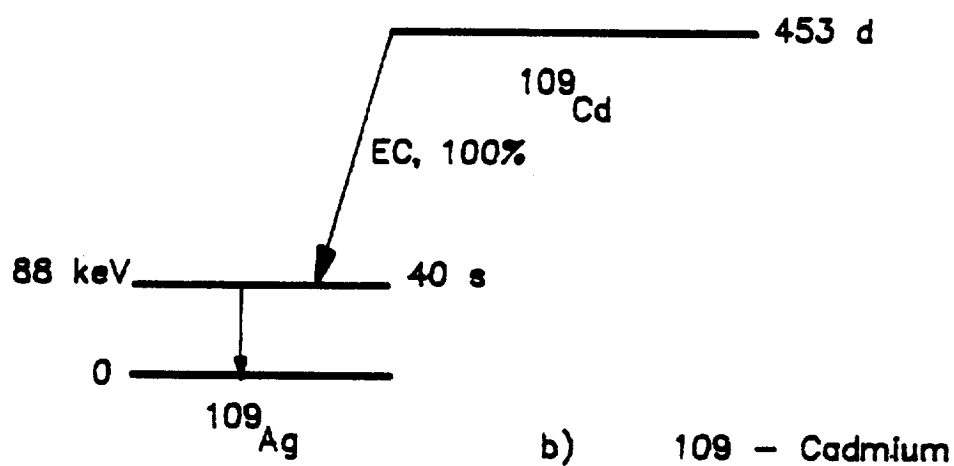
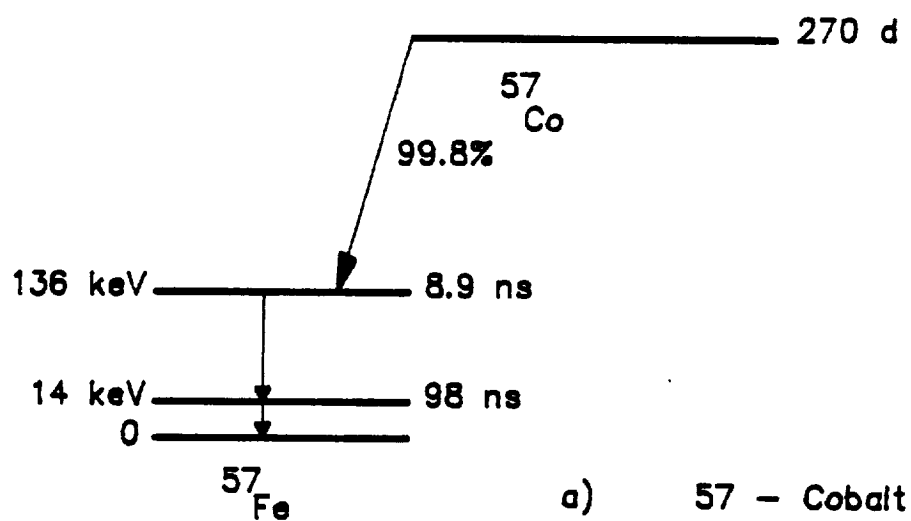


Figure 2. Simplified Decay Schemes of ^{57}Co , ^{109}Cd and ^{51}Cr

The values of η were determined from the standard gamma ray sources for a particular multichannel analyzer set-up.

Let I^+ be the ion beam current impinging on the target surface. The number of ions, N_i , incident on the target per unit time is given by

$$N_i = \frac{I^+}{q} \quad (4)$$

where q is the charge of an ion. If the exposure period is t_e and the sputtering yield is S , then the total number of sputtered atoms, N_s , is given by

$$N_s = \frac{SI^+t_e}{q} \quad (5)$$

Since the sputtered atoms have sticking probabilities of nearly 1 on metal substrates, it is assumed that all sputtered atoms are collected on the foil surrounding the target. The number of radioactive atoms on the foil, N_r , is then given by

$$N_r = \gamma N_s \quad (6)$$

where γ is the percentage of the radioactive atoms on the target at the time of the measurement. γ decreases with time

and is determined by

$$\gamma = \gamma_0 e^{-\lambda T} \quad (7)$$

where γ_0 is the percentage of radioactive atoms on the target at the time of electroplating, λ is the decay constant of the radioactive tracer atoms, and T is the elapsed time between electroplating the sample and the day the data were taken. The decay constant is related to the half-life, $t_{1/2}$, by

$$\lambda = \frac{0.693}{t_{1/2}} \quad (8)$$

Substituting the value of N_s from Eq. 5 into Eq. 6, we get

$$N_r = \frac{\gamma S I^+ t_0}{q} \quad (9)$$

The number of atoms disintegrating per unit time, N_d , in the sputtered sample is given by

$$N_d = \lambda N_r \quad (10)$$

Substituting value of N_r from Eq. 9 into Eq. 10, we get

$$N_d = \frac{\lambda \gamma S I^* t_o}{q} \quad (11)$$

If the sputtered atoms produce a count of N_c gamma rays under the photoelectric peak over a counting time t_c , then

$$\eta N_d = \frac{N_c}{t_c} \quad (12)$$

Substituting the value of N_d from Eq. 11 in Eq. 12, the expression for the sputtering yield can be obtained by

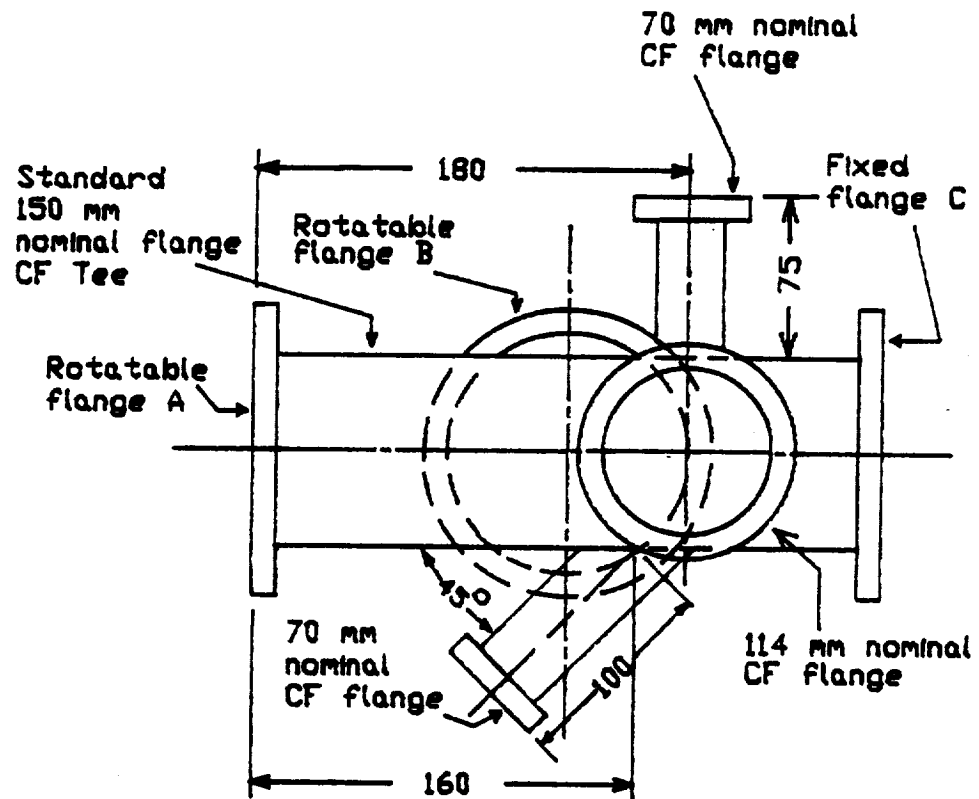
$$S = \frac{N_c q}{\eta \lambda \gamma I^* t_o t_c} \quad (13)$$

Substituting the value of γ from Eq. 7 in Eq. 13, we have the expression for S as

$$S = \frac{N_c q}{\eta \lambda (\gamma_o e^{-\lambda T}) I^* t_o t_c} \quad (14)$$

Vacuum System

The vacuum chamber was 100 mm in diameter and had six ports. A schematic view of the vacuum chamber is shown in Fig. 3. The ion gun entered from the left through a 150-mm CF (conflat flange) port. The bottom 150-mm CF flange was connected to the turbomolecular pump. The ionization gauge



TOP VIEW

Drawing not to scale
All dimensions are in mm

Figure 3. Schematic View of the Vacuum Chamber

was mounted on the 70-mm CF port. The target-collector assembly was introduced from the right port by a linear motion feedthrough which was connected to the vacuum chamber through a 150-mm CF to 70-mm CF adapting nipple. A viewport was attached to the 114-mm port. The vacuum chamber had a 70-mm CF auxiliary port at a 45° angle which was not used in the present set up. A 170 l/s turbomolecular pumping system was chosen to provide the required vacuum conditions because of its operational simplicity. The pressure inside the vacuum chamber was measured by a hot cathode ionization gage.

Ion Gun

Due to safety issues associated with working with mercury, we decided to use ions of elements other than mercury in our study. A low energy ion gun, built by Kimball Physics Inc., was used in the present investigation. The ion gun had the dual capability of generating both alkali metal ions and ions of noble gases such as argon, krypton and xenon. The ion gun was designed to generate ions from 10 to 500 eV. The alkali metal was generated as needed from a built-in unit by a solid-solid chemical reaction and was then surface ionized and evaporated. The resulting ion beam could be generated down to low energies with low energy spread. The ion gun used a refractory oxide cathode to generate ions by electron impact ionization of gases admitted through an auxiliary gas inlet.

The ion gun was mounted on a 150-mm CF flange. It

extended to a length of 178 mm beyond the 150-mm CF flange. The gun diameter was 25 mm at the flange and necked upto 32 mm at 76 mm from the flange. All necessary voltages to drive the ion gun were contained in a modular power supply unit. The gases entered the ion gun through a port multiplexer attached to a 70-mm CF flange which was bolted onto the 150-mm CF flange. Research grade purity argon or xenon contained in cylinders was metered into the ion gun through a leak valve. A schematic diagram of the gas flow unit is shown in Fig. 4.

The broad beam diameter of the ion beam was about 3 mm whereas the focused ion beam had a spot diameter of about 1 mm at a distance of 20 mm from the exit plane of the ion gun. The ion current was measured by a Faraday cup which was mounted below the ion gun. It could be actuated pneumatically to intercept the ion beam at a distance of 6 mm from the exit plane of the ion gun. The Faraday cup was interfaced with an electrometer to provide the ion current reading. A picture of the ion gun is shown in Fig. 5.

Target-Collector Assembly

The target materials were electroplated on the tip of copper specimens which behaved as substrates (Fig. 6). Substrates of two different sizes were used in our experiments. The substrate A (Fig. 6a) was 4.8 mm in diameter whereas the substrate B (Fig. 6b) had a diameter of 11.1 mm. The surface of the target was elliptical in shape with an area of 25.8

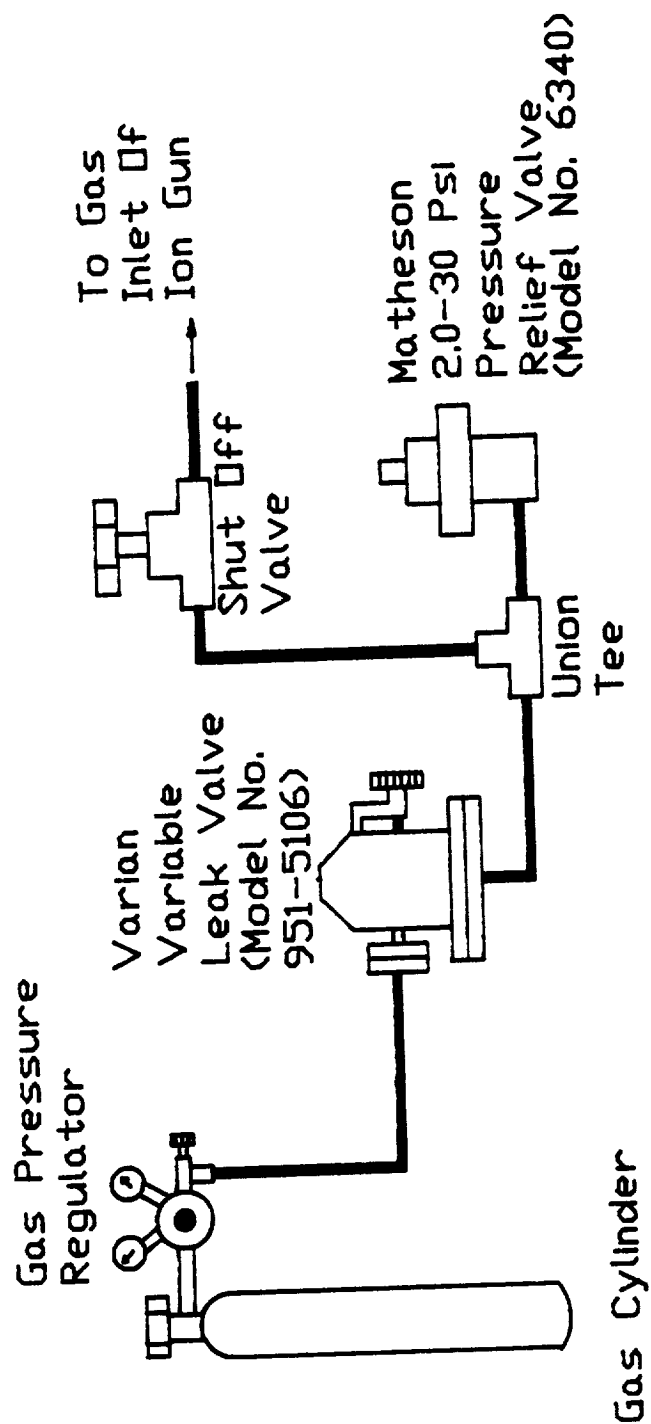


Figure 4. Schematic of the Gas Flow Unit

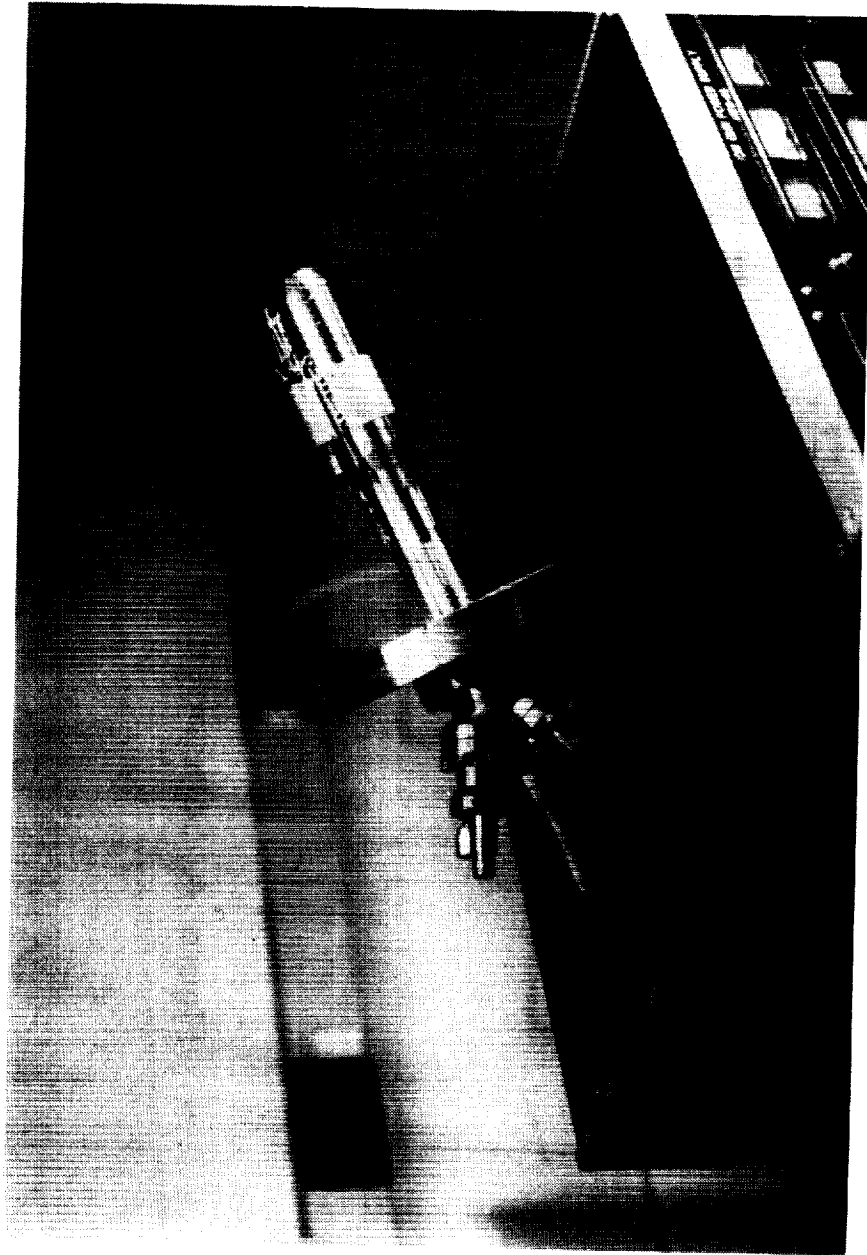
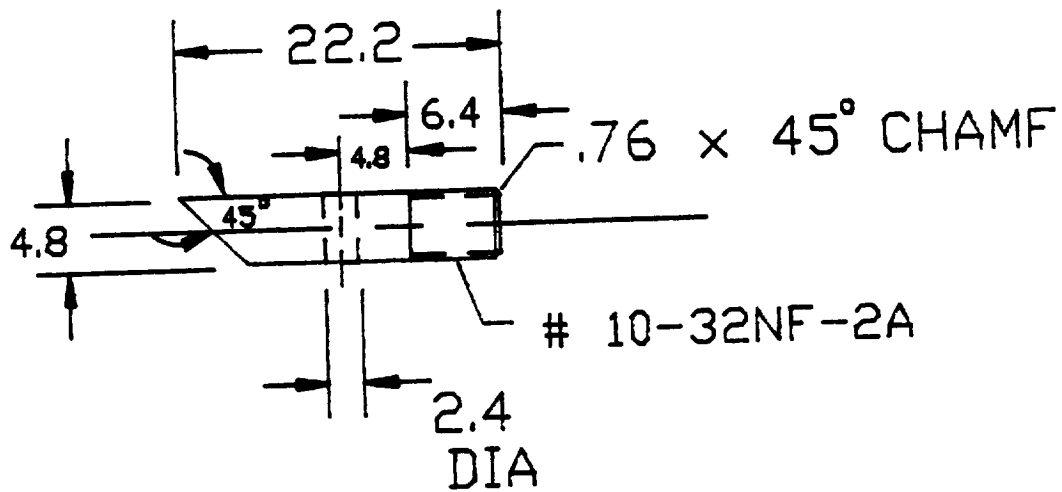
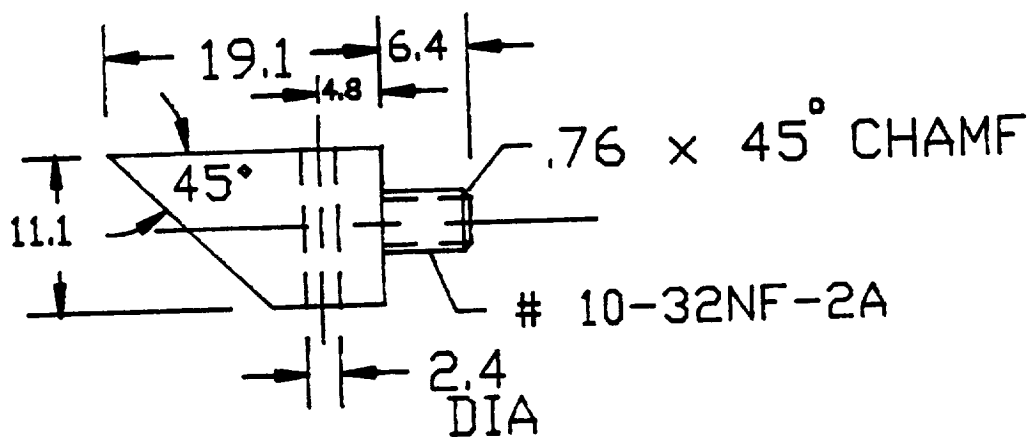


Figure 5. Ion Gun

ORIGINAL PAGE
BLACK AND WHITE PHOTOGRAPH



a) Substrate A



b) Substrate B

All dimensions are in mm

Figure 6. Substrate Dimensions

mm² for substrate A and 137 mm² for substrate B. Cobalt electroplated on substrate A and cesium ions were used initially to characterize the experimental set-up. The sputtering yields with argon and xenon ions were measured using targets electroplated on substrate B. The surface density of the electroplated material was approximately 50 µg/cm².

The copper substrate was completely surrounded by a hollow cylinder whose internal diameter was 22 mm. The inside of the cylinder was lined with a thin metal foil. The ion gun and the target were separated by 20 mm. A schematic diagram of the ion gun and the target-collector assembly using the substrate A is shown in Fig. 7. A picture of the overall experimental set up is shown in Fig. 8.

Experimental Procedure

A run was started by initially pumping down the vacuum chamber to a base pressure of 2×10^{-7} Torr to remove as much of the ambient reactive gases as possible. After achieving the chamber base pressure, the ion gun was turned on to either produce cesium ions or ions of noble gases such as argon or xenon.

To produce cesium ions at the desired energy, the proper energy voltage was first set on the ion gun power supply unit. Then appropriate voltages were set on the other electrodes of the ion gun. Next, the cesium source voltage and current were adjusted to obtain the maximum possible beam current at the desired energy. The Faraday cup was activated

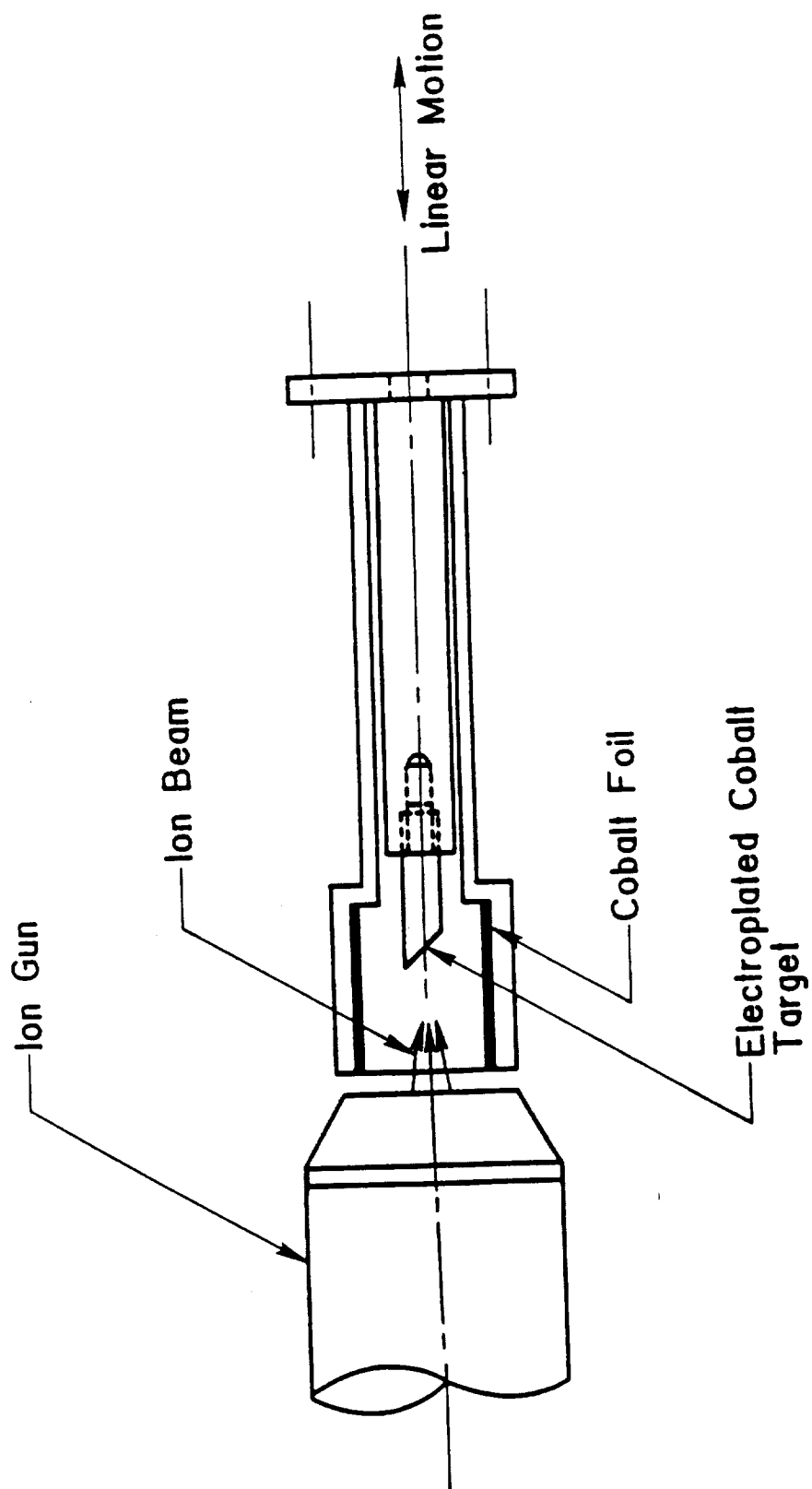


Figure 7. Schematic of the Ion Gun and the Collector Assembly

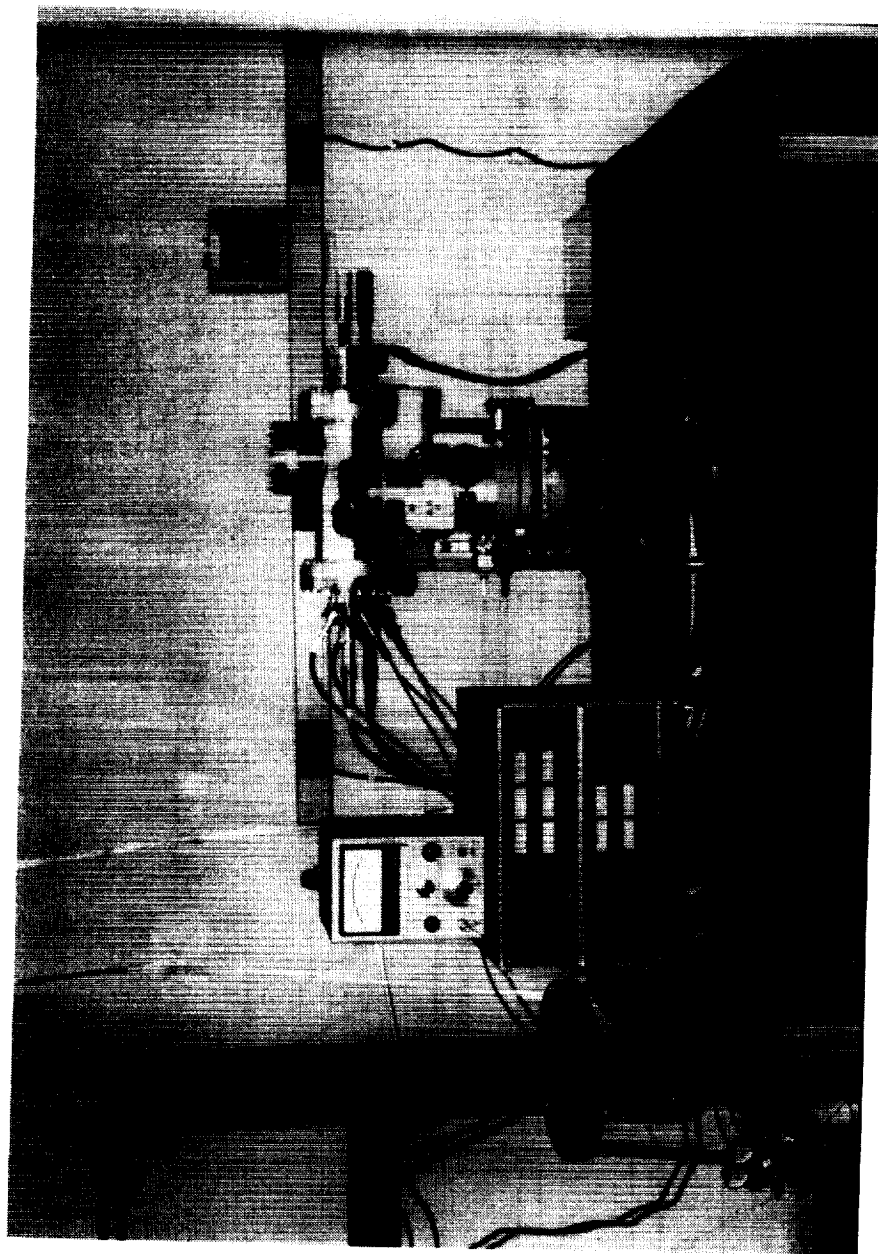


Figure 8. Overall Experimental Set Up

ORIGINAL PAGE
BLACK AND WHITE PHOTOGRAPH

to measure the ion current. The focus voltage was finally set to optimize the ion beam current.

For generating ions of noble gases, the shut-off valve in the gas feed line was opened to admit either argon or xenon into the vacuum chamber. The gas flow was metered by a leak valve and the chamber pressure was stabilized at 2×10^{-5} Torr. The appropriate energy voltage and the electrode voltages were then set on the ion gun power supply unit. Next, the electron beam voltage and current were set to ionize the gas. The source voltage was adjusted to produce the maximum possible beam current at the desired energy. Finally, the focus voltage was set to optimize the ion beam current.

After removing the Faraday cup from the ion beam path, the target-collector assembly was moved forward to bring the mid-region of the target surface at the focal point of the ion beam. The distance between the ion gun and the target was monitored by the micrometer on the linear motion feed-through. After the desired exposure, the target was retracted and the ion current was measured again. After switching off the ion gun power supply and the vacuum pump, the target-collector assembly was removed from the vacuum chamber. The foil was taken out from the collector sleeve and placed in a 12-mm diameter, 75-mm long glass tube. The glass tube was placed inside the well of the multichannel analyzer to count the disintegration rate of the radioactive atoms deposited on the foil. The background subtracted count

under the photoelectric peak was representative of the number of radioactive atoms deposited on the foil due to sputtering. A new metal foil was placed in the collector sleeve and the assembly was put back on the vacuum chamber for the next run.

RESULTS AND DISCUSSION

Calibration of the Multichannel Analyzer

The linearity of the 1024-channel analyzer was tested by using reference gamma ray sources which provide distinct photoelectric peaks. The gamma ray sources used for the linearity check and the associated gamma ray energies are listed in Table 1. The channel at which the photoelectric peak appears is plotted against the energy of the gamma rays in Fig. 9 which indicates the linearity of the multichannel analyzer.

Table 1. Radioisotopes and Energies of the Photoelectric Peaks Used in Calibrating the Multichannel Analyzer

Radioactive Isotope	Energy of the Photoelectric Peak (keV)
^{109}Cd	88
^{57}Co	122
^{51}Cr	320
^{137}Cs	662
^{60}Co	1173 and 1332

A typical gamma ray energy spectra of ^{57}Co , ^{109}Cd and ^{51}Cr reference sources are shown in Fig. 10. A background energy spectrum is also included in the same figure for

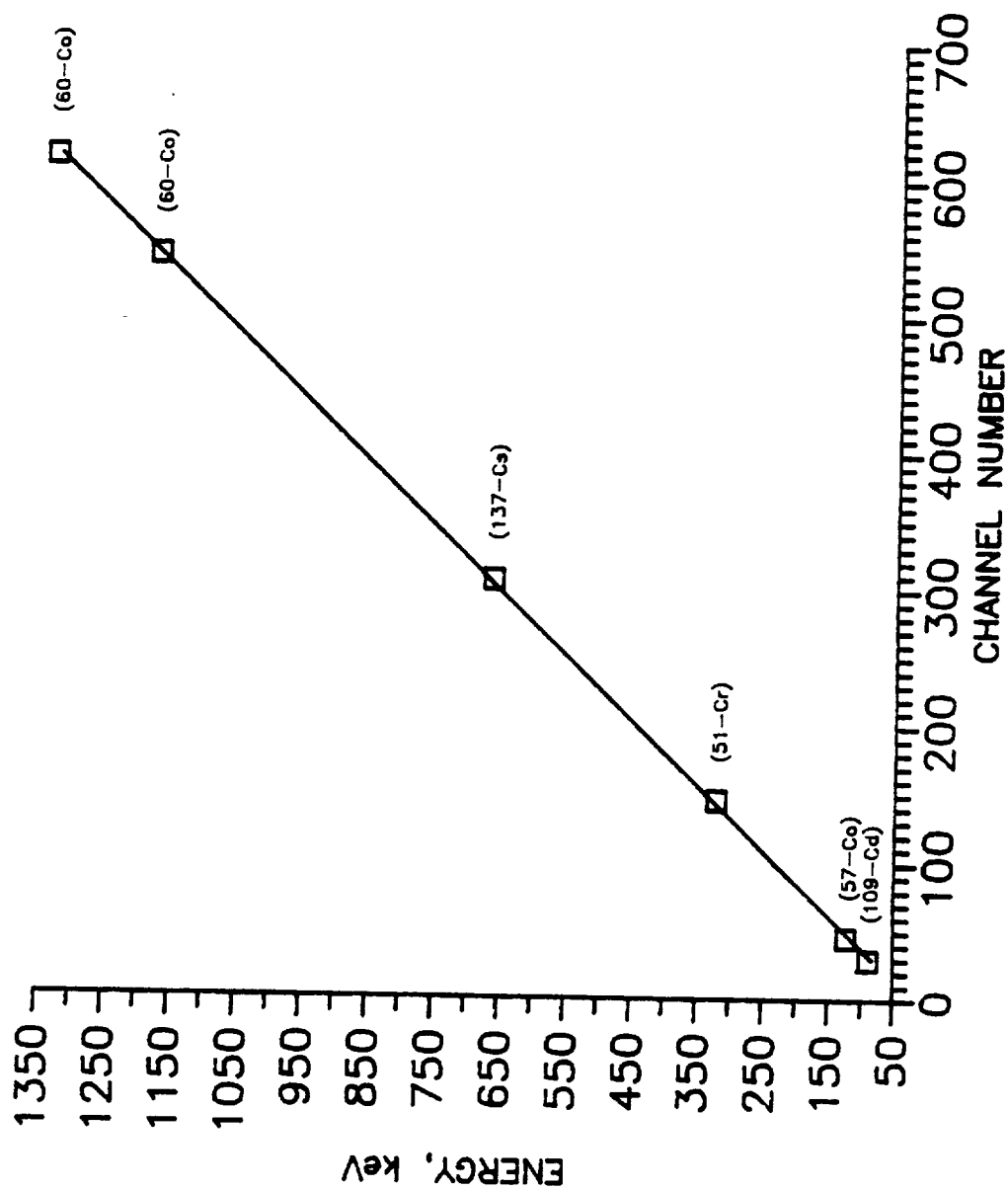
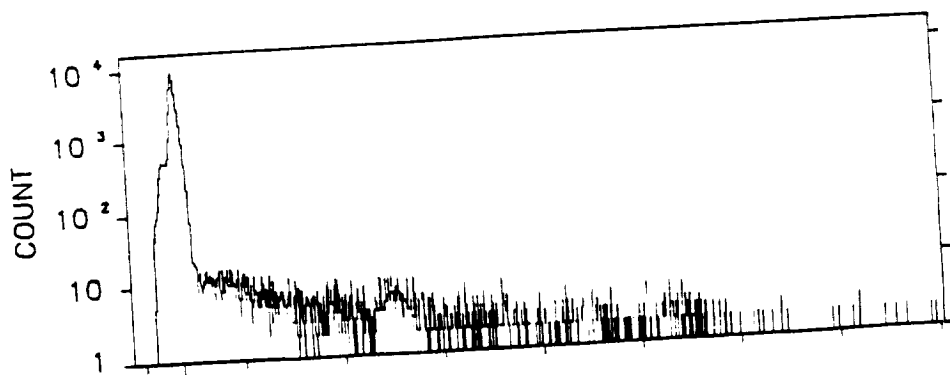
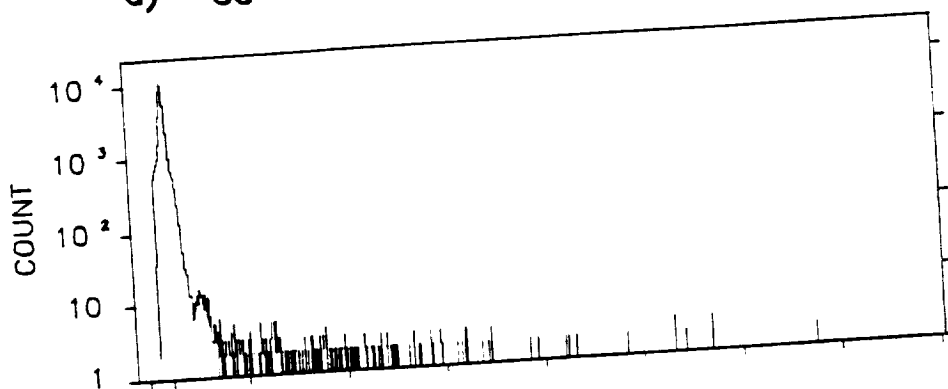


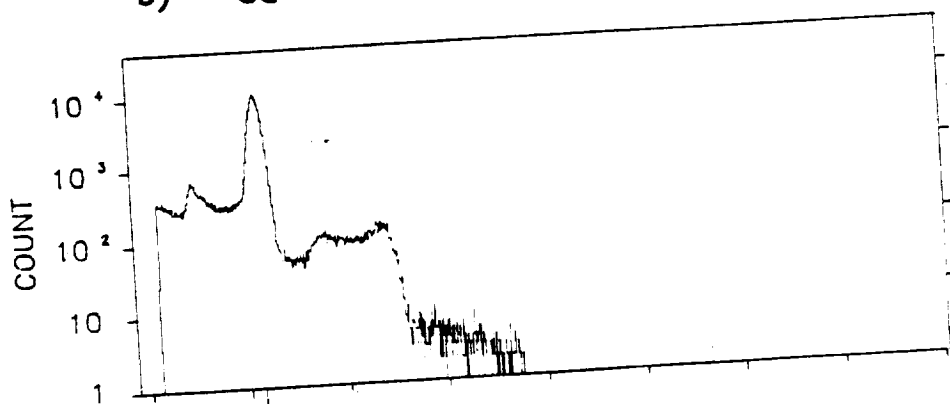
Figure 9. Location of the Photoelectric Peak in the Mutichannel Analyzer



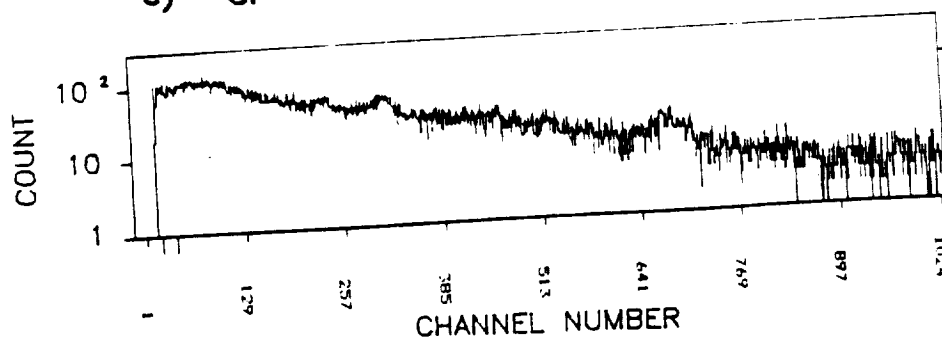
a) ^{57}Co



b) ^{109}Cd



c) ^{51}Cr



d) Background Spectrum

Figure 10. Gamma Ray Energy Spectra of ^{57}Co , ^{109}Cd , ^{51}Cr and a Typical Background Spectrum

comparison.

The efficiency with which a photoelectric peak was counted was determined in the following manner. First, two channels were selected, one on each side of the location of the photoelectric peak. A background count was then obtained between these two channels for 5 minutes. Next, a gamma ray reference source was placed inside the well of the scintillation detector and the total count was obtained between the same channels for 5 minutes. The background subtracted total count determined the number of gamma rays which deposited sufficient energy in the scintillation detector to be counted between the two channels. Since the total number of gamma rays emitted by the reference source over this time period was known, the counting efficiency of the photoelectric peak was determined by dividing the background subtracted count with the known disintegration from the reference source. The counting efficiencies of the photoelectric peaks are given in Table 2.

Table 2. Counting Efficiency of the Photoelectric Peaks of ^{57}Co , ^{109}Cd and ^{51}Cr

Radioactive Tracer	Photoelectric Peak Counting Efficiency (%)
^{57}Co	84
^{109}Cd	3.12
^{51}Cr	5.54

System Characterization

A. Vacuum System Operation : After the initiation of the pumpdown, a vacuum level of 1×10^{-6} Torr was reached in about 30 minutes. During the initial testing of the vacuum system, an equilibrium pressure of 5×10^{-7} Torr was reached after 2 hours (Fig. 11). Since the turbomolecular pumping system was expected to provide a vacuum level lower than 5×10^{-7} Torr, we suspected that a leak existed in the vacuum chamber. After a leak check, a minute depression was found on the knife edge of the left 150-mm flange of the vacuum chamber. To minimize the leak, a special O-ring shaped metal gasket was put on this flange. With the O-ring gasket in place a base pressure of 2×10^{-7} Torr was reached in about 90 minutes.

B. Ion Gun Operating Characteristics : The operating characteristics of the ion gun were established using cesium ions generated from a built-in unit and a cobalt target electroplated on substrate A. The distance between the ion gun and the target was controlled by a micrometer-operated linear motion feedthrough on which the target-collector assembly was mounted. The ion beam could be focused at a distance of about 20 mm from the exit plane of the ion gun. To optimize the ion gun-target distance, sputtering yields of cobalt were measured by 500 eV cesium ions by slightly varying the ion gun-target distance around 20 mm. The relative sputtering yield is plotted in Fig. 12 against distance. It is observed that the sputtering yield is maximized

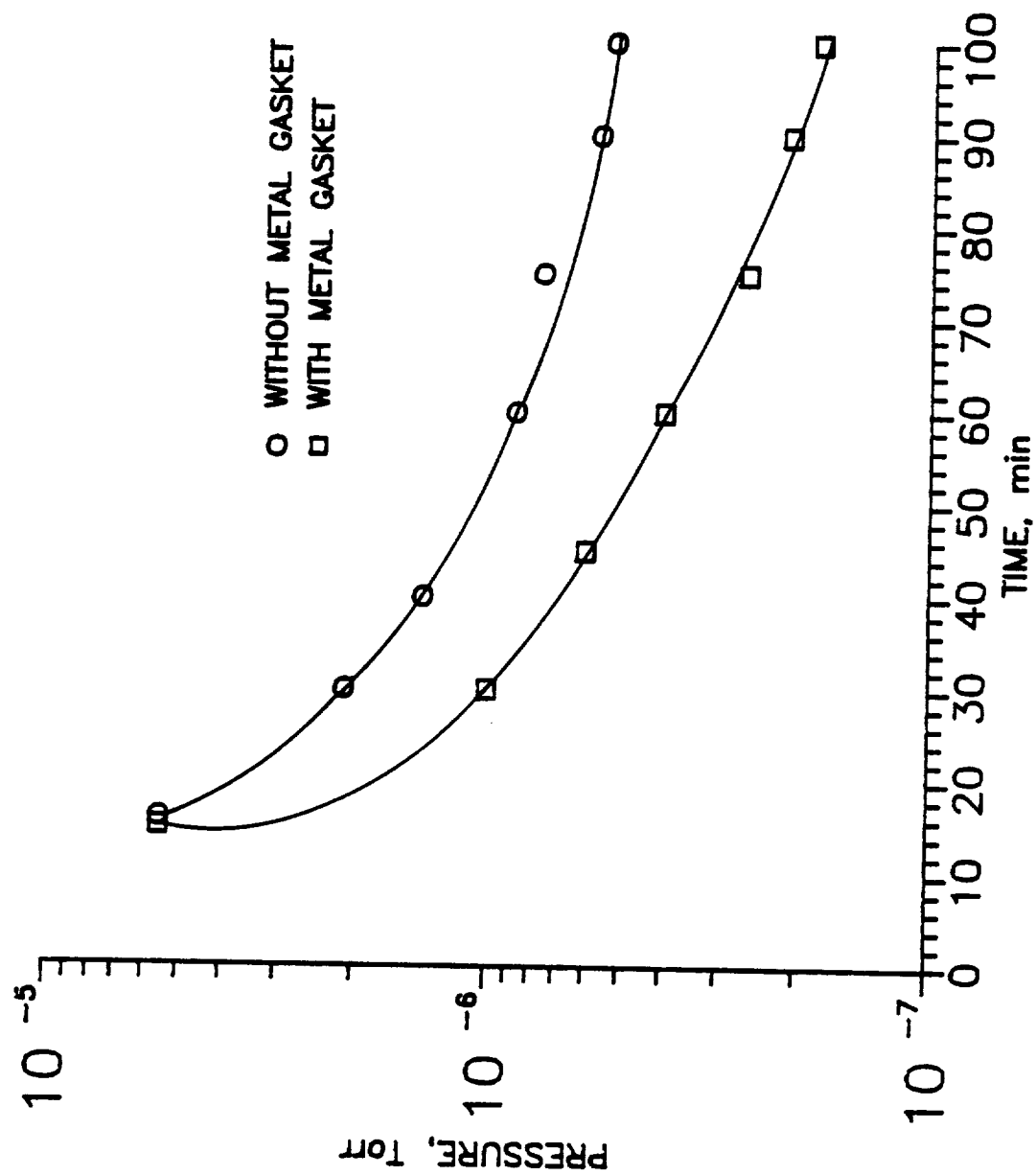


Figure 11. Typical Pumpdown Curve for the Vacuum Chamber

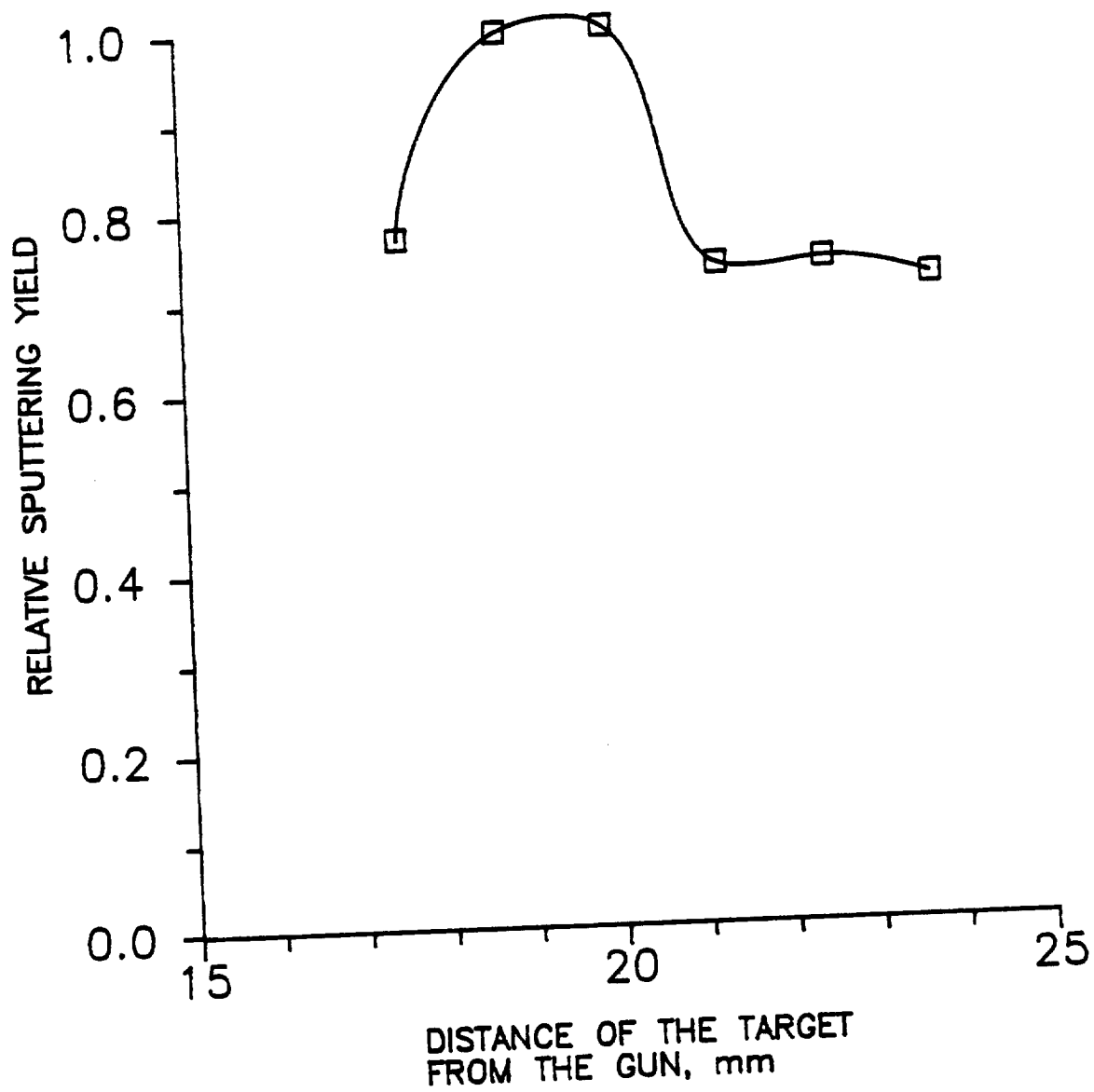


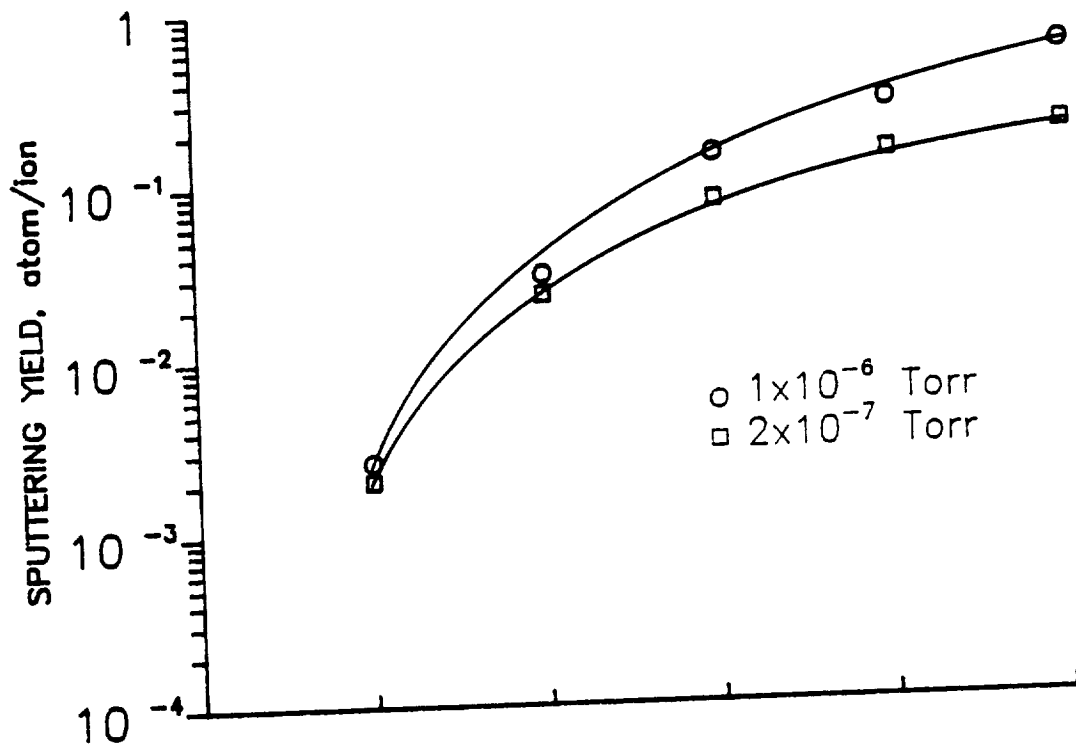
Figure 12. Variation of the Sputtering Yield With Ion Gun-Target Distance

when the ion gun and the target were separated by a distance of 19.5 mm. This distance was maintained in all measurements.

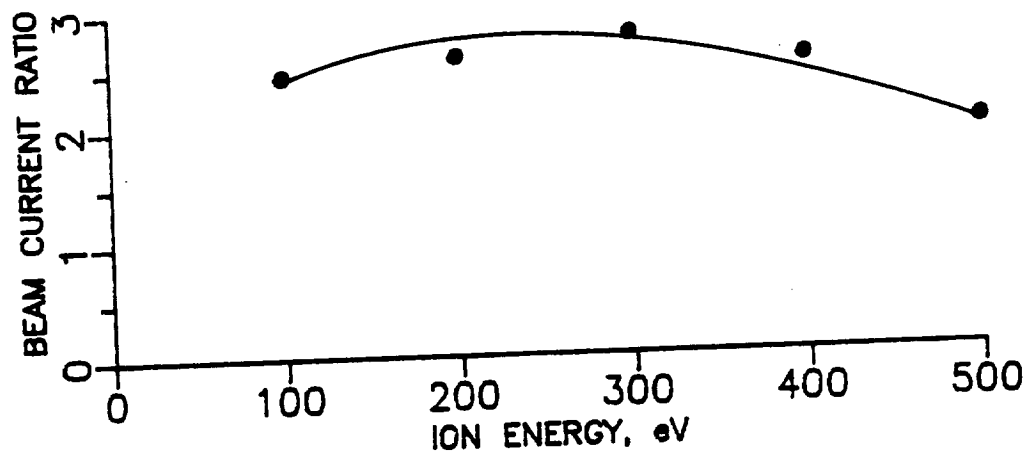
C. Effect of Pressure on Sputtering by Cesium Ions :

Initially, the sputtering yields of cobalt by cesium ions were measured at an operating pressure of 1×10^{-6} Torr. Since the cesium ions are generated from a solid source, chamber pressure is not affected by the operation of the ion source. After the metal O-ring gasket was installed the sputtering yields were measured at an operating pressure of 2×10^{-7} Torr. At the lower pressure, the yields were found to be lower than those measured at the higher pressure (Fig. 13a). The difference in the sputtering yields was small at low energies and difference was increased with increasing ion energy upto 500 eV which was the maximum energy that could be obtained from the ion gun. It should be noted though that the cesium beam current was considerably reduced due to the depletion of the source by the time the runs were taken at 2×10^{-7} Torr. The ratio of the ion beam currents at various ion energies at the two pressures are shown in the same graph (Fig. 13b). No simple relationship appears to exist between the yield, the operating pressure, the beam current and the ion energy.

D. Cesium Ion Beam Characteristics : Since the cesium source was a built-in unit of the ion gun, the ion current produced by the source decreased as the source was depleted. The maximum ion current obtained was $1.2 \mu\text{A}$.



a) Sputtering Yields



b) Ratio of Beam Currents

Figure 13. Effect of Pressure and Current on the Sputtering Yield of Cobalt by Cesium Ions

The sputtering yields of cobalt by cesium ions at 100, 200, 300, 400 and 500 eV are presented in Fig. 14. The target was bombarded for times varying from 2 to 10 minutes. For comparison, the sputtering yield of cobalt by mercury ions reported by Wehner is also presented, although the experiments were performed under different conditions [24]. The sputtering yield values obtained by Wehner are 2 to 5 times higher than those obtained from our experiment.

The discrepancy in the sputtering yield values can be attributed not only to the different ion species but also to the vacuum chamber pressure and the ion current densities at which these data were taken. Wehner's experiments were performed with the target immersed in a low-pressure mercury plasma discharge at an operating pressure of about 1×10^{-3} Torr and 5 mA/cm^2 ion current density. The highest current density obtained in our experiments with cesium ions was 0.15 mA/cm^2 based on a 1-mm beam diameter at the target surface.

Below 100 eV, difficulties were encountered with the operation of the cesium ion beam. Hence no measurements were made with cesium ions at energies lower than 100 eV.

Sputtering Yields of Cobalt by Argon and Xenon Ions

A. Operating Pressure : To determine the operating pressure for sputtering with noble gases, yields of cobalt were measured at 2×10^{-5} and 2×10^{-6} Torr with argon ions. As seen in Fig. 15, the sputtering yields at the two gas pressures

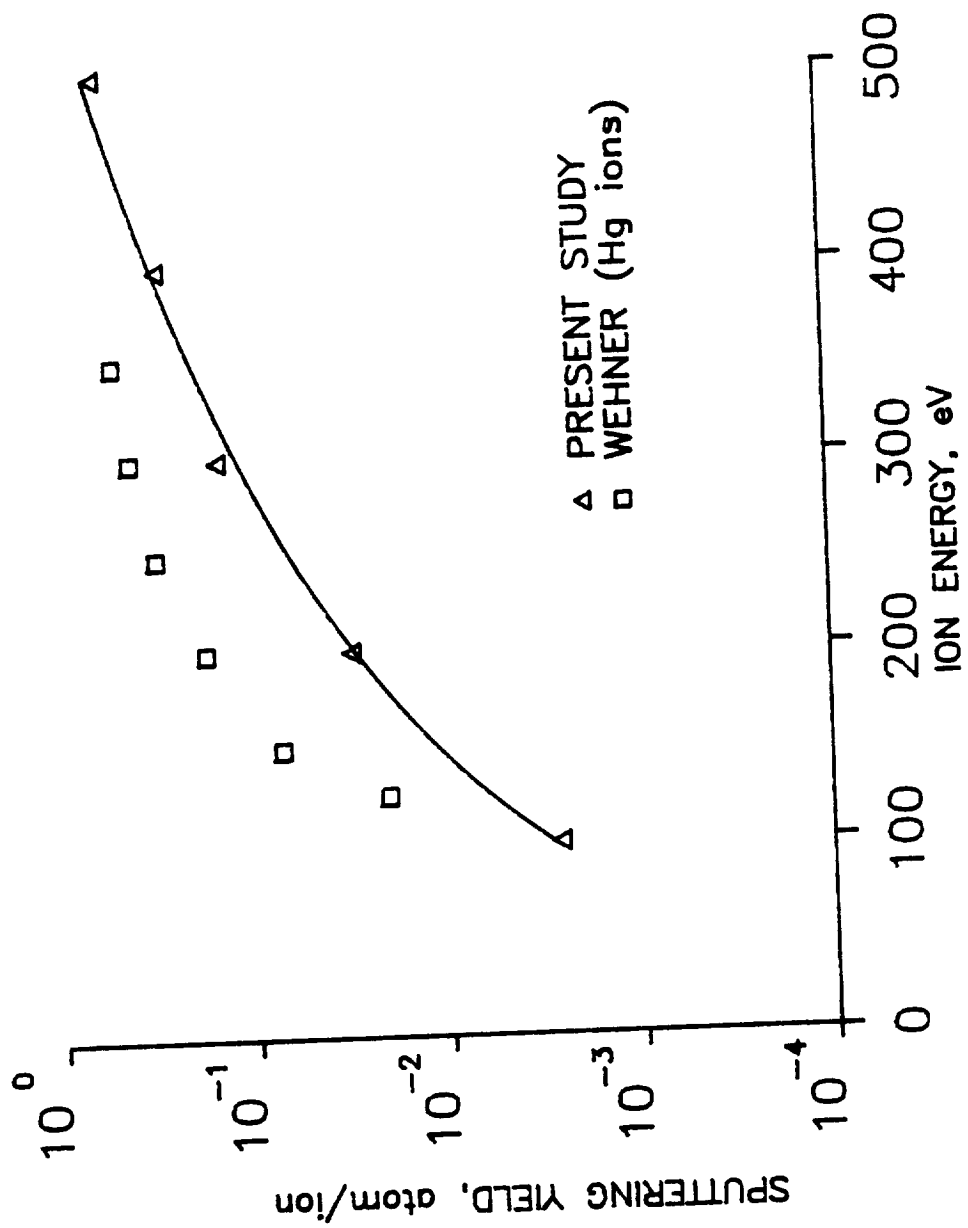


Figure 14. Sputtering Yield of Cobalt by Cesium Ions

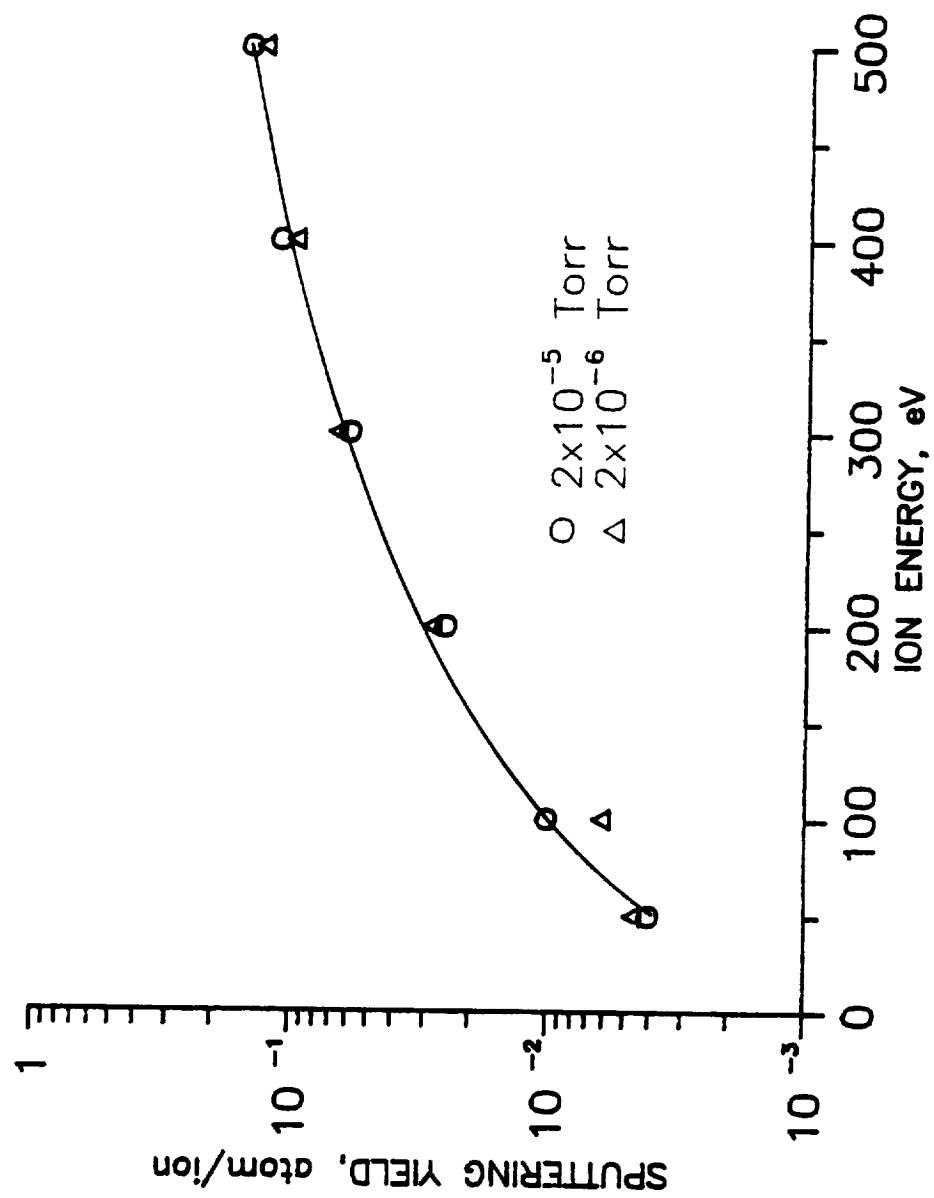


Figure 15. Sputtering Yield of Cobalt by Argon Ions at Different Operating Pressures

are comparable. However, the maximum ion current obtainable at 2×10^{-6} Torr was 3 to 4 times lower than those obtained at 2×10^{-5} Torr except for the 100 eV run where the ion current was about 10 times lower. In view of this, we decided to make all subsequent runs at 2×10^{-5} Torr.

B. Sputtering Yield by Argon Ions : The sputtering yield of cobalt by argon ions from 10 to 500 eV is presented in Fig. 16. The yield from 10 to 100 eV at 10 eV intervals is presented in the inset of the same figure. The beam current ranged from 0.022 to 0.84 μ A. The target was bombarded for times varying from 2 minutes at 500 eV to 5 hours at 10 eV. For comparison, the sputtering yield of cobalt by argon ions reported by Stuart and Wehner [20] having energies from 25 to 300 eV is also presented in the same figure. The yields obtained by Stuart and Wehner are significantly higher at higher ion energies (as high as 25 times at 200 eV) than those measured in this experiment.

The discrepancy in the sputtering yield values is likely due to the low ion current densities at which our data were taken as well as the formation of some impurities, such as oxides, on the target surface. Stuart and Wehner's experiments were performed in an argon plasma discharge at an ion current density of about 40 mA/cm². The highest ion current density obtained in our experiments was 0.1 mA/cm². Stuart and Wehner also had the target surface sputter cleaned before each run. In our experiments the surface could not be sputter cleaned before each run due to the use of a single

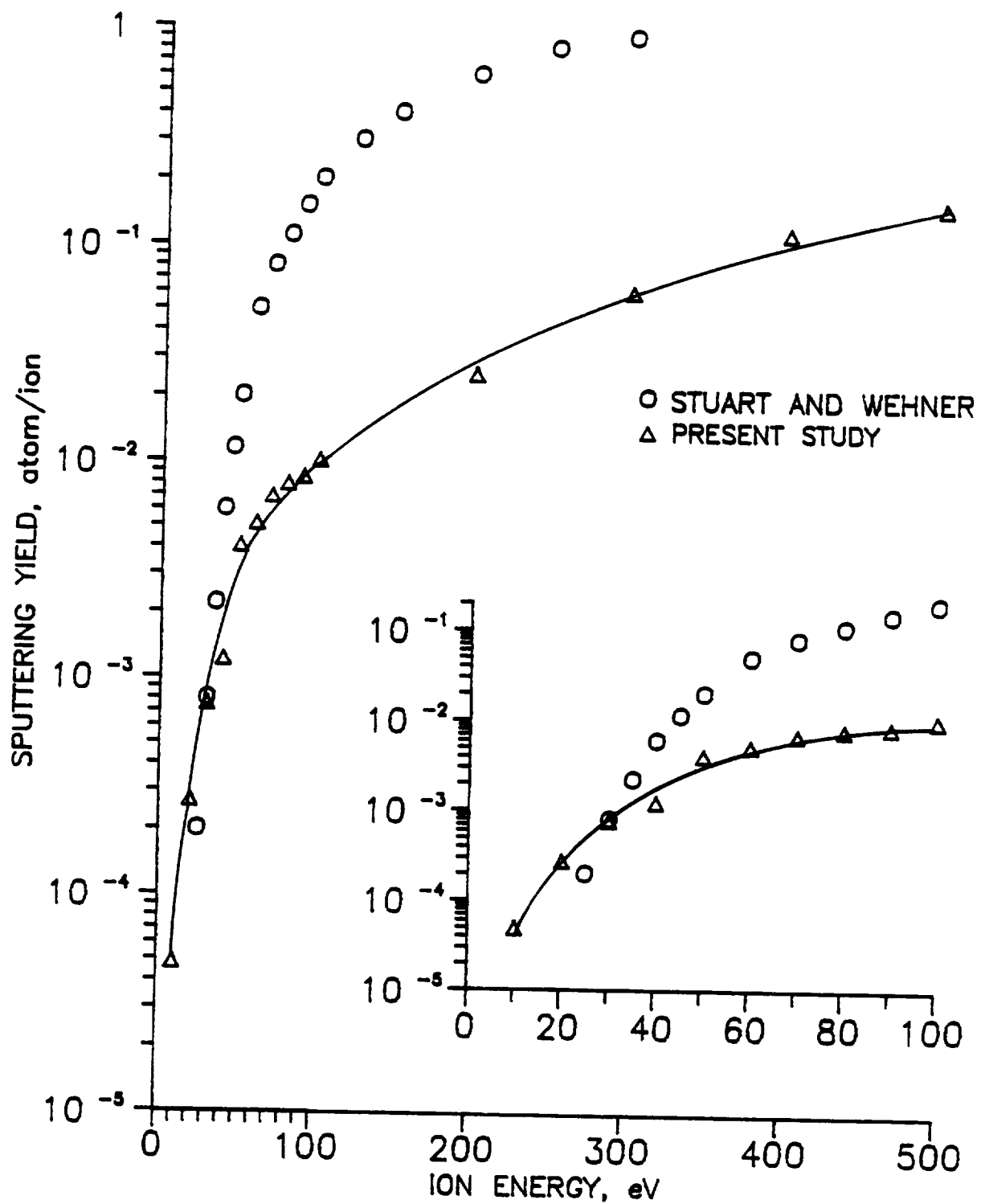


Figure 16. Sputtering Yield of Cobalt by Argon Ions

collector sleeve surrounding the target.

When the ratio of the two sputtering yields are plotted against the ion energy, an intriguing feature is revealed (Fig. 17). The ratio of the two yields decreases monotonically as the ion energy is decreased, eventually becoming close to 1 at 30 eV and lower than 1 at 25 eV. The reason for this behavior is not clear.

C. Sputtering Yield by Xenon Ions : The sputtering yield of cobalt by xenon ions is shown in Fig. 18. The yield from 10 to 100 eV at 10 eV intervals is presented in the inset. The ion beam current varied from 0.0135 to 0.64 μA and the time of exposure ranged from 2 minutes to 3 hours. It is observed that the xenon ions sputter at a higher rate compared to argon ions with same energies.

For comparison, yields of cobalt by xenon reported by Rosenberg and Wehner [19] at 100, 200, 300 and 400 eV are plotted in Fig. 18. Since only a few Co-Xe⁺ data points are available, the sputtering yields of cobalt by mercury ions reported by Askerov and Sena [22] are also plotted in the same figure. It should be noted though that yields by mercury ions are usually 3 to 5 times lower than those by xenon ions. It can be seen that the yields reported by Rosenberg and Wehner using an ion current density of 2 to 8 mA/cm² are 6 to 12 times higher. The yields obtained by Askerov and Sena are higher at higher energies and the yield-energy curve displays the same trend of coming closer and eventually becoming lower at lower energies.

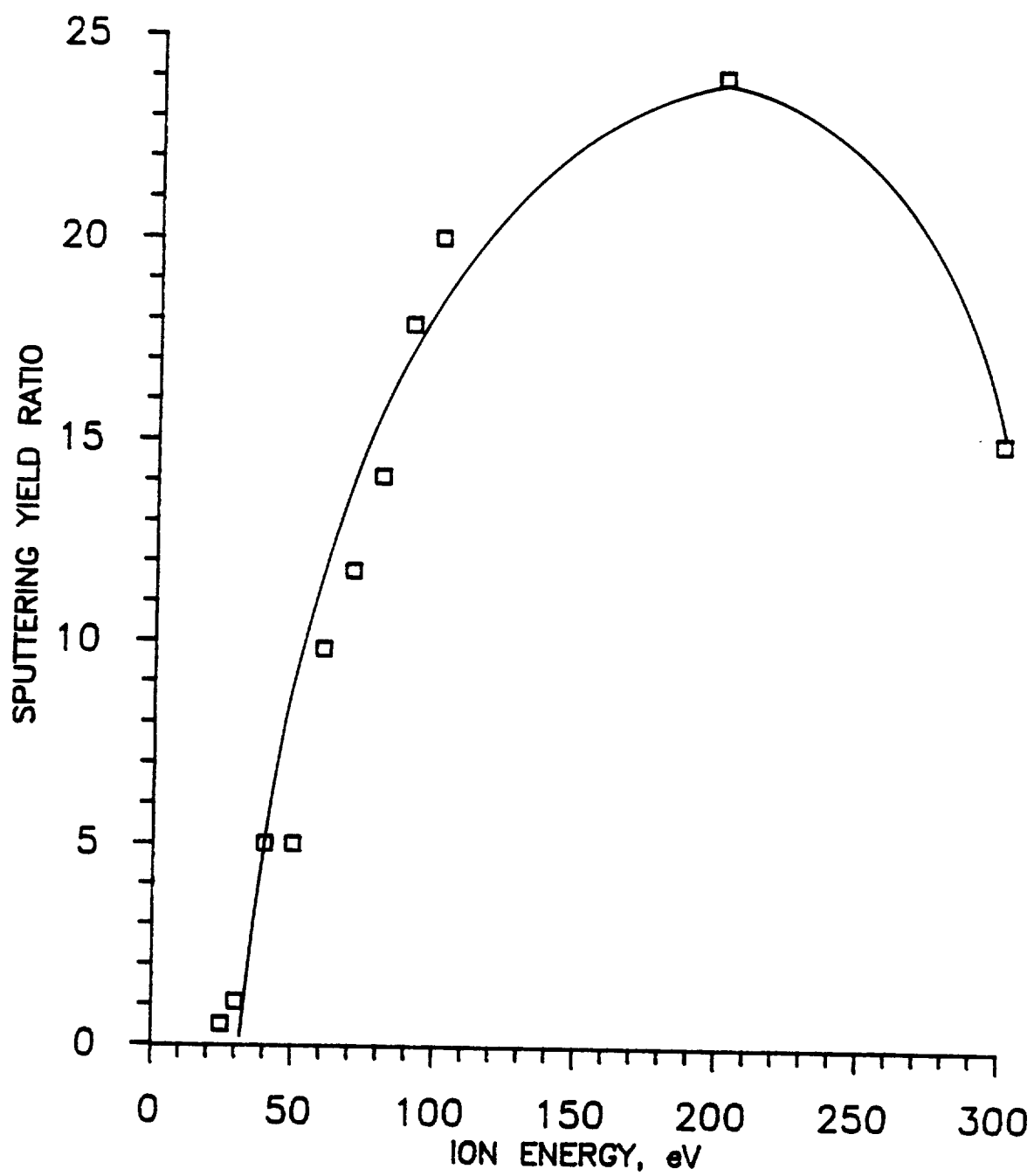


Figure 17. Sputtering Yield Ratio of Cobalt by Argon Ions

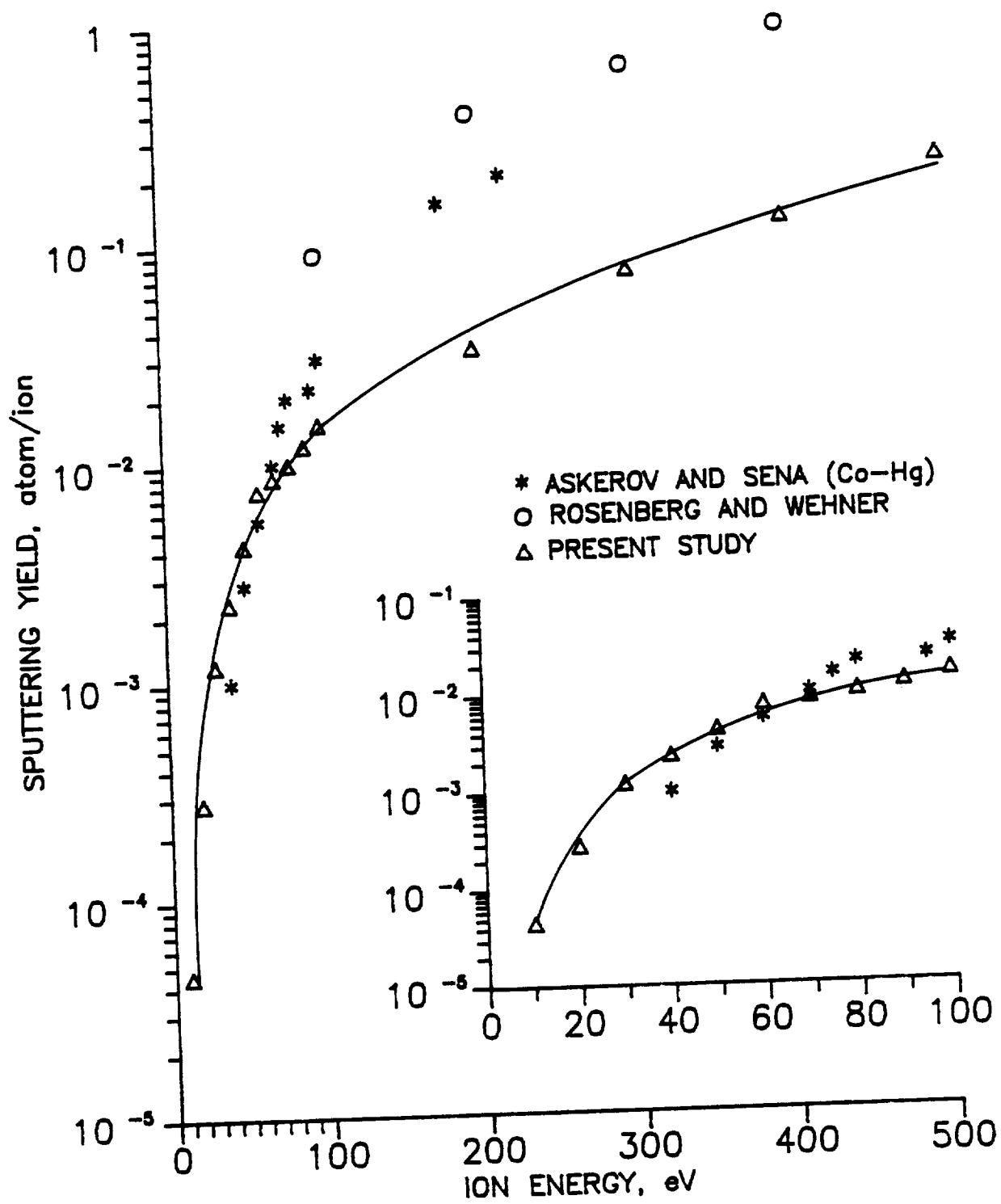


Figure 18. Sputtering Yield of Cobalt by Xenon Ions

D. Sputtering Yields Near Threshold Energy : On a semi-logrithmic plot, the sputtering yields by both argon and xenon ions display similar pattern. From 500 eV downwards upto about 50 eV ion energy, the yields decrease at a slower rate compared to those below 50 eV when the yields fall rapidly. If the yields near the threshold energies are plotted on a linear scale it is seen that the yield-energy curves become concave, deviating from the expected straight line form (Figs. 19 and 20). The uncertainty in the sputtering yield values in our experiments is estimated to be $\pm 15\%$ and is indicated by error bars in these figures. This trend in the sputtering yield near threshold energy was observed in an earlier investigation of low-energy sputtering of nickel and cobalt by mercury and argon ions using a plasma discharge [16]. The yields of nickel mixed with 1% ^{60}Co by argon ions obtained in that study are plotted in Fig. 21 along with our data for comparison. It is interesting to note that if the low-energy sputtering yield of cobalt by argon obtained by Stuart and Wehner [20] are also plotted on a linear scale, a similar trend is observed (Fig. 19).

Sputtering Yields of Cadmium by Argon and Xenon Ions

A. Sputtering Yields by Argon and Xenon Ions : The sputtering yields of cadmium by argon ions from 10 to 500 eV are presented in Fig. 22. The yields from 10 to 100 eV at 10 eV intervals are presented in the inset. The ion beam current ranged from 0.025 to 0.57 μA . The time of exposure ranged

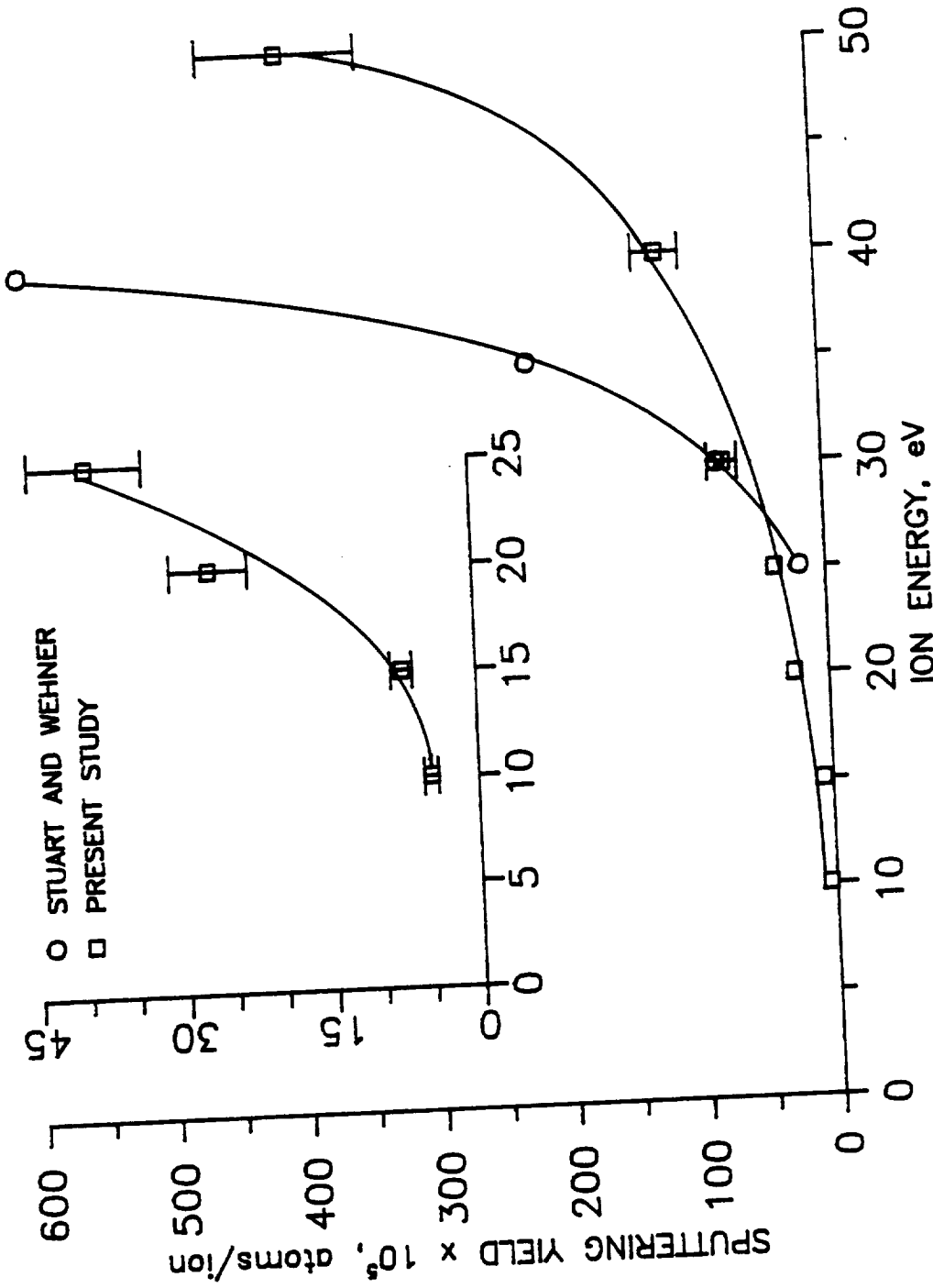


Figure 19. Sputtering Yield of Cobalt by Argon Ions Near Threshold Energy

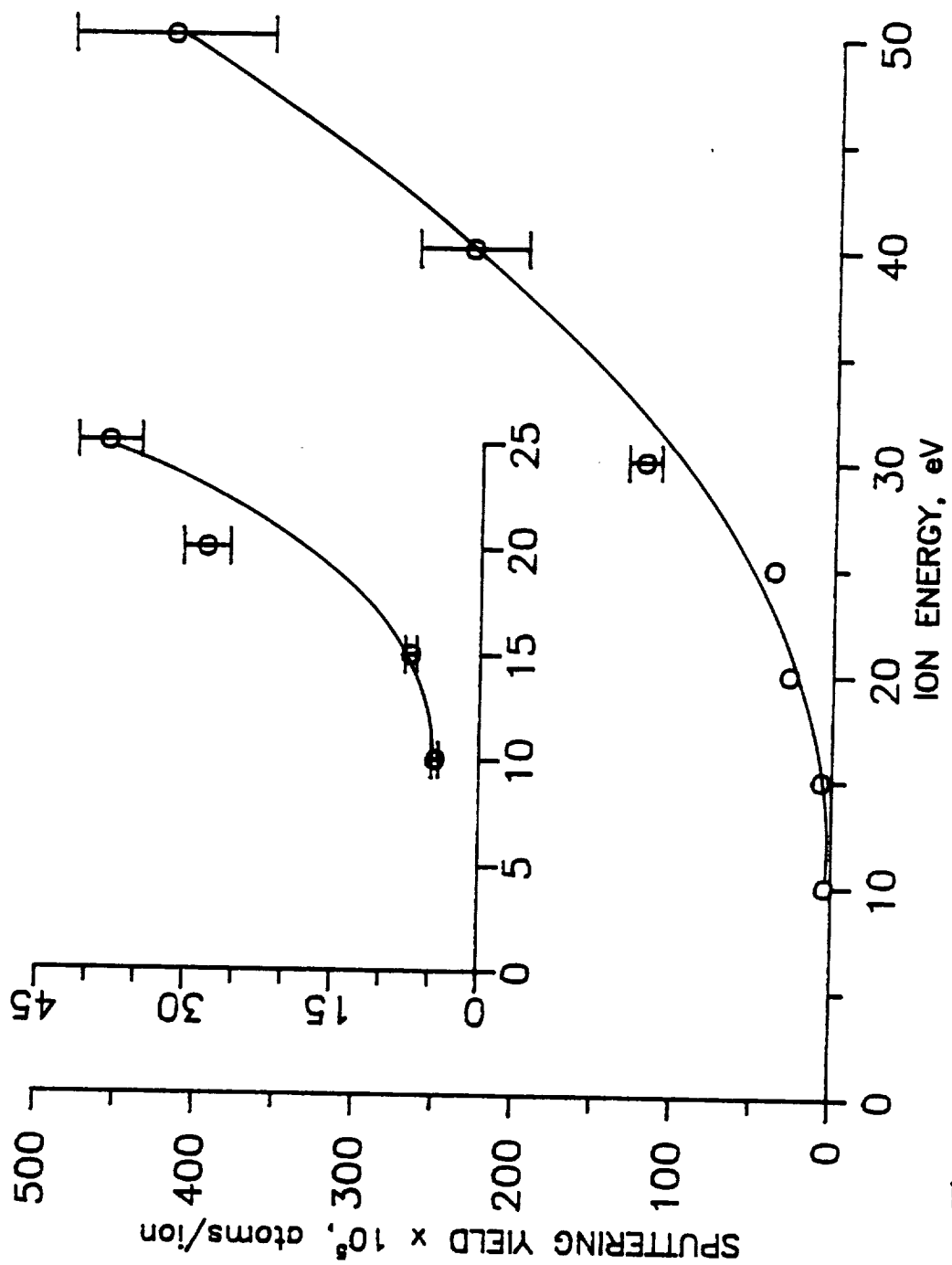


Figure 20. Sputtering Yield of Cobalt by Xenon Ions Near Threshold Energy

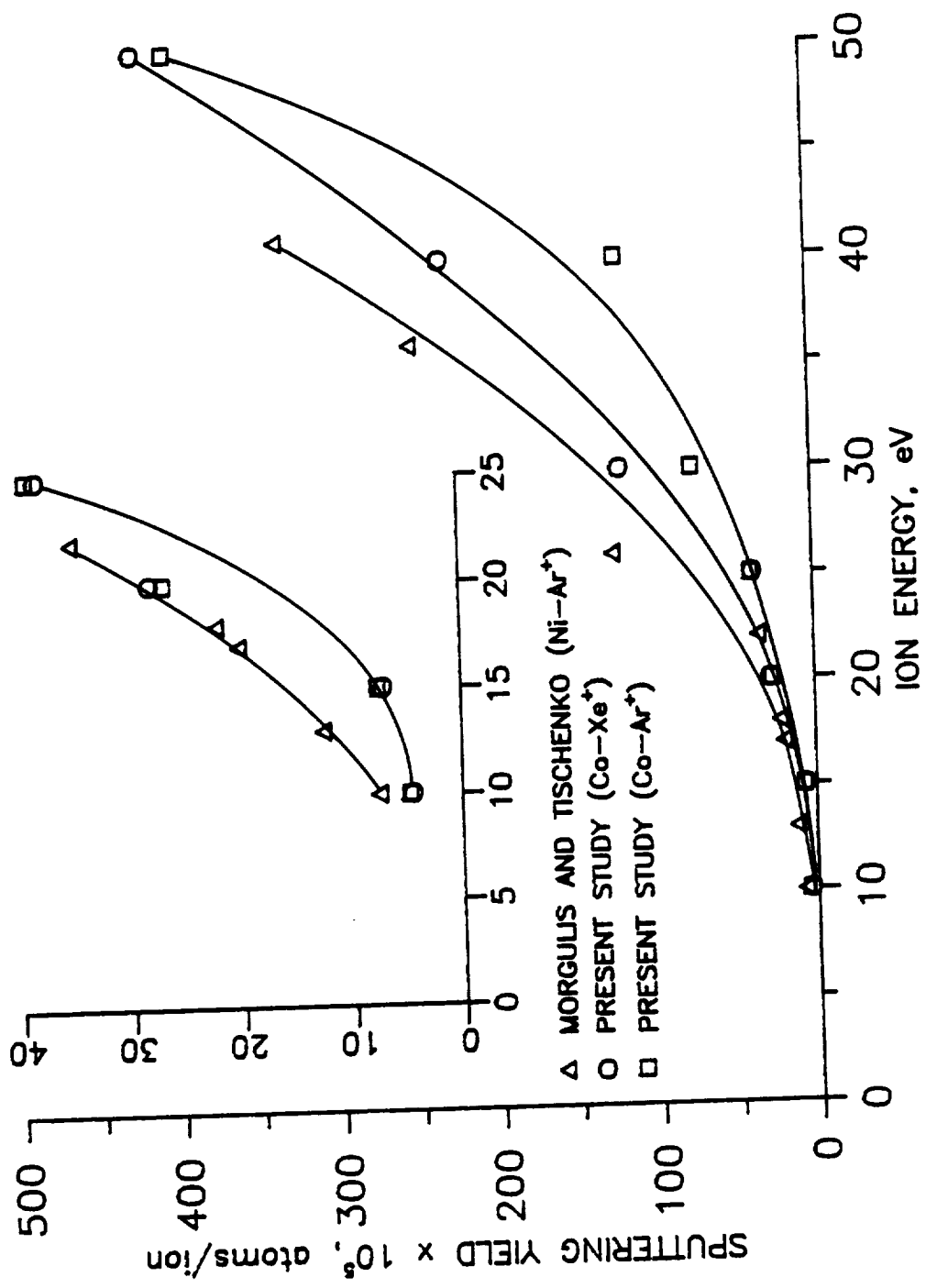


Figure 21. Sputtering Yield of Cobalt by Argon and Xenon Ions Compared with Yield of Nickel by Argon Near Threshold Energy

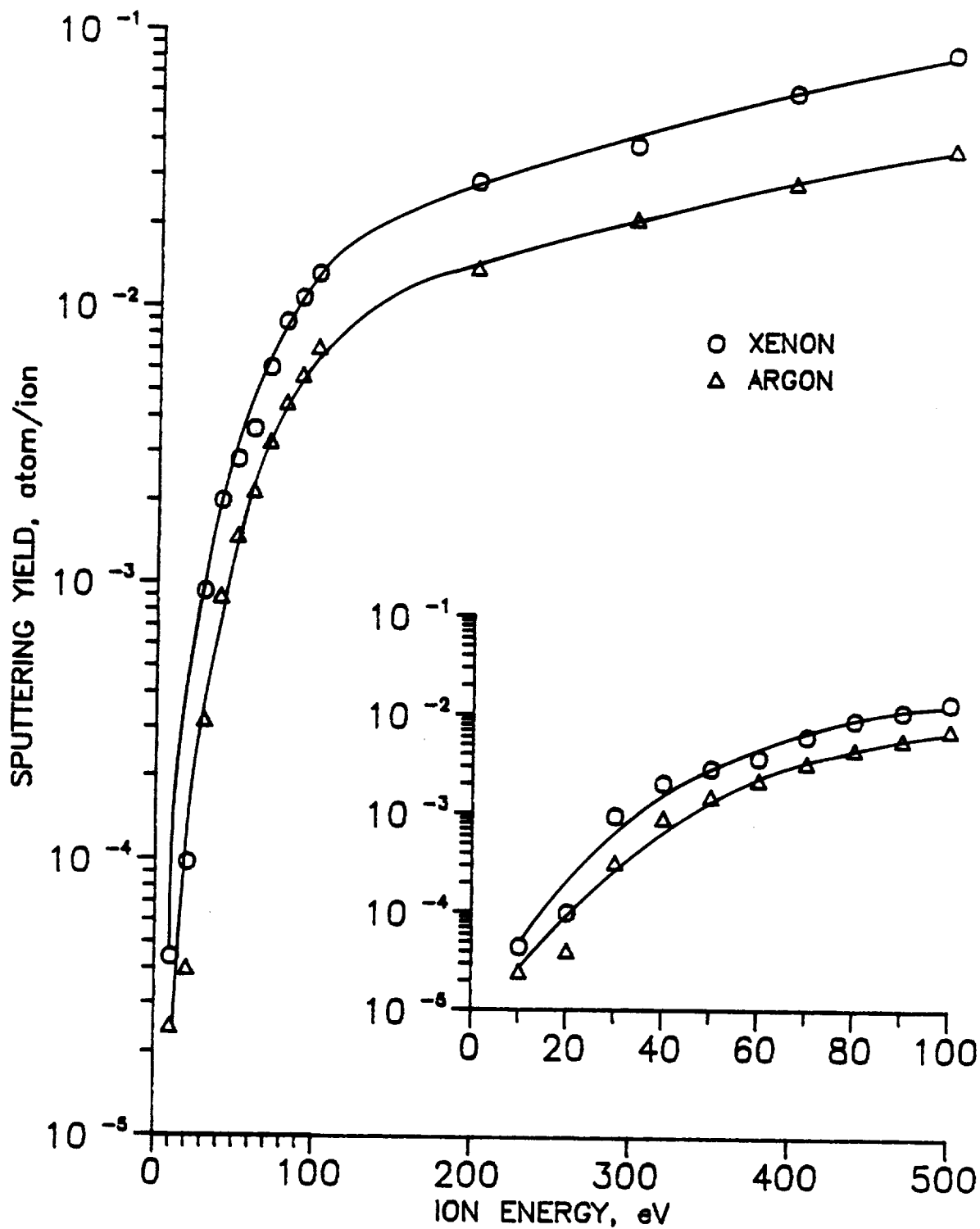


Figure 22. Sputtering Yield of Cadmium by Argon and Xenon Ions

from 5 minutes at 500 eV to 7 hours at 10 eV.

Fig. 22 also provides the sputtering yields of cadmium by xenon ions. The ion beam current varied from 0.017 to 0.7 μA and the time of exposure ranged from 2 minutes to 5 hours. Xenon ions are observed to sputter at a higher rate than argon ions with same energies. However, we could not compare the yield of cadmium obtained from our experiments with those of other researchers since low-energy sputtering data of cadmium are not available in the open literature.

The sputtering yields of cadmium near the threshold energies are plotted in Fig. 23 on a linear scale. Here also the yield-energy curves reveal the concave nature but each curve appears as a combination of two straight lines with the knee at 25 eV for argon ions and 20 eV for xenon ions.

Sputtering Yields of Chromium by Argon and Xenon Ions

A. Sputtering Yield by Argon Ions : The sputtering yield of chromium by argon ions from 20 to 500 eV is shown in Fig. 24. The yield from 20 to 100 eV at 10 eV intervals is presented in the inset. The ion beam current ranged from 0.028 to 0.62 μA . The time of exposure ranged from 2 minutes at 500 eV to 2 hours at 20 eV. For comparison, the sputtering yield of chromium by argon ions reported by Stuart and Wehner [25] having energies from 25 to 350 eV is also presented.

The yields obtained by Stuart and Wehner agree reasonably well with our values. The agreement between the

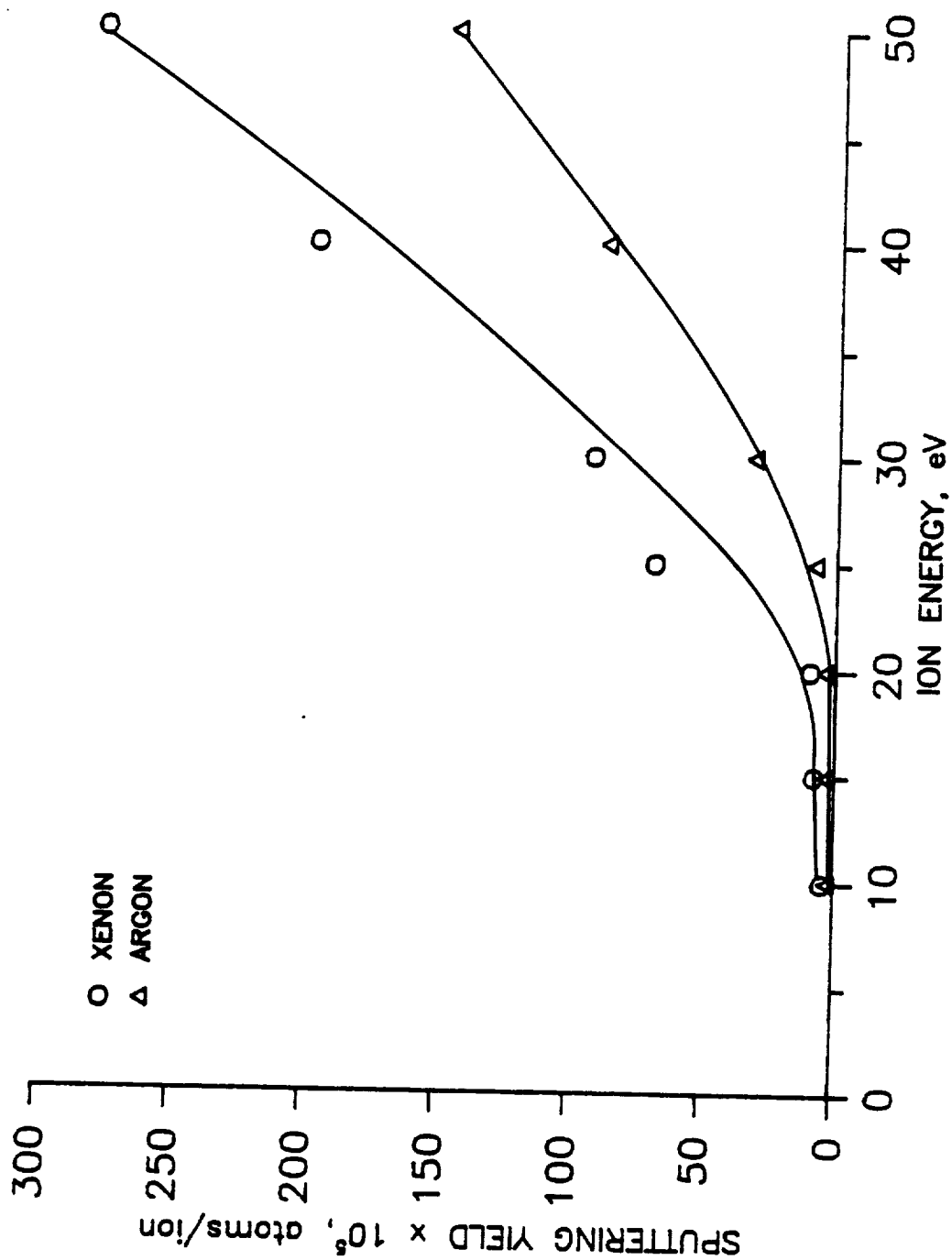


Figure 23. Sputtering Yield of Cadmium by Argon and Xenon Ions Near Threshold Energy

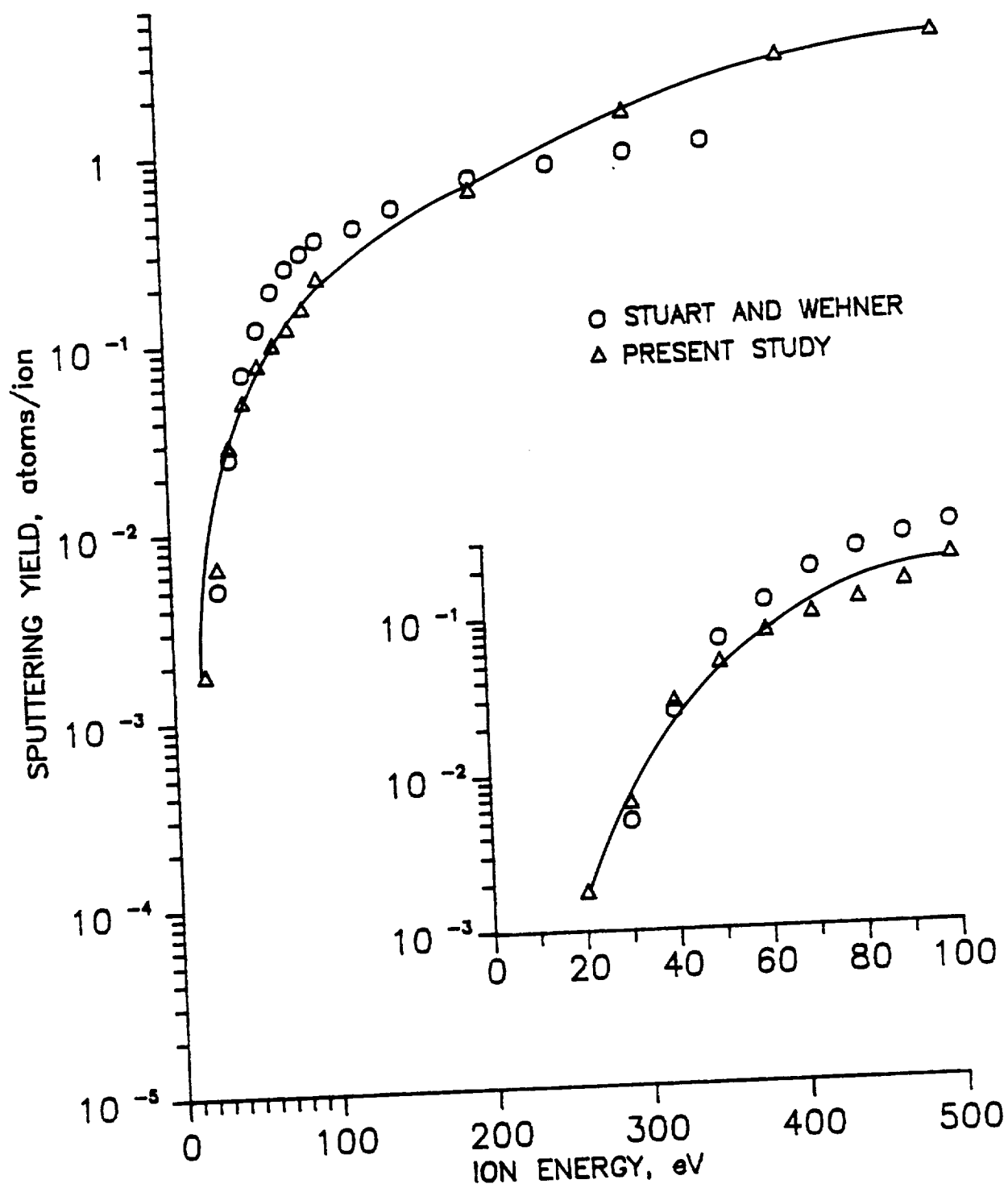


Figure 24. Sputtering Yield of Chromium by Argon Ions

two sets of data is surprising. Not only are the current densities at least an order of magnitude higher in Stuart and Wehner's experiment but also our yields of cobalt and cadmium indicate relatively low values compared to those obtained from the experiments using plasma discharge.

B. Sputtering Yield by Xenon Ions : The sputtering yield of chromium by xenon ions are shown in Fig. 25. The yields from 20 to 100 eV at 10 eV intervals are presented in the inset. The ion beam current varied from 0.042 to 0.72 μA and the time of exposure ranged from 2 minutes to 2 hours. Again the xenon ions are observed to sputter at a higher rate compared to argon ions with same energies.

For comparison, yields of chromium by xenon reported by Rosenberg and Wehner [19] at 100, 200, 300 and 400 eV are plotted in Fig. 25. Although only four data points are available for comparison, it can be seen that our yields are 3 to 4 times higher than those reported by Rosenberg and Wehner. The reasons for obtaining comparatively higher sputtering yields for chromium in our experiments are not clear.

C. Sputtering Yields Near Threshold Energy : The sputtering yields of chromium near the threshold energies are plotted in Fig. 26 on a linear scale. The concave nature of the yield-energy curve is also clearly visible in this graph. For chromium we could not measure any sputtering yield below 20 eV for argon ions and below 15 eV for xenon ions. The activity of the target was rather low when these runs were made due to the short half-life (27.7 days) of

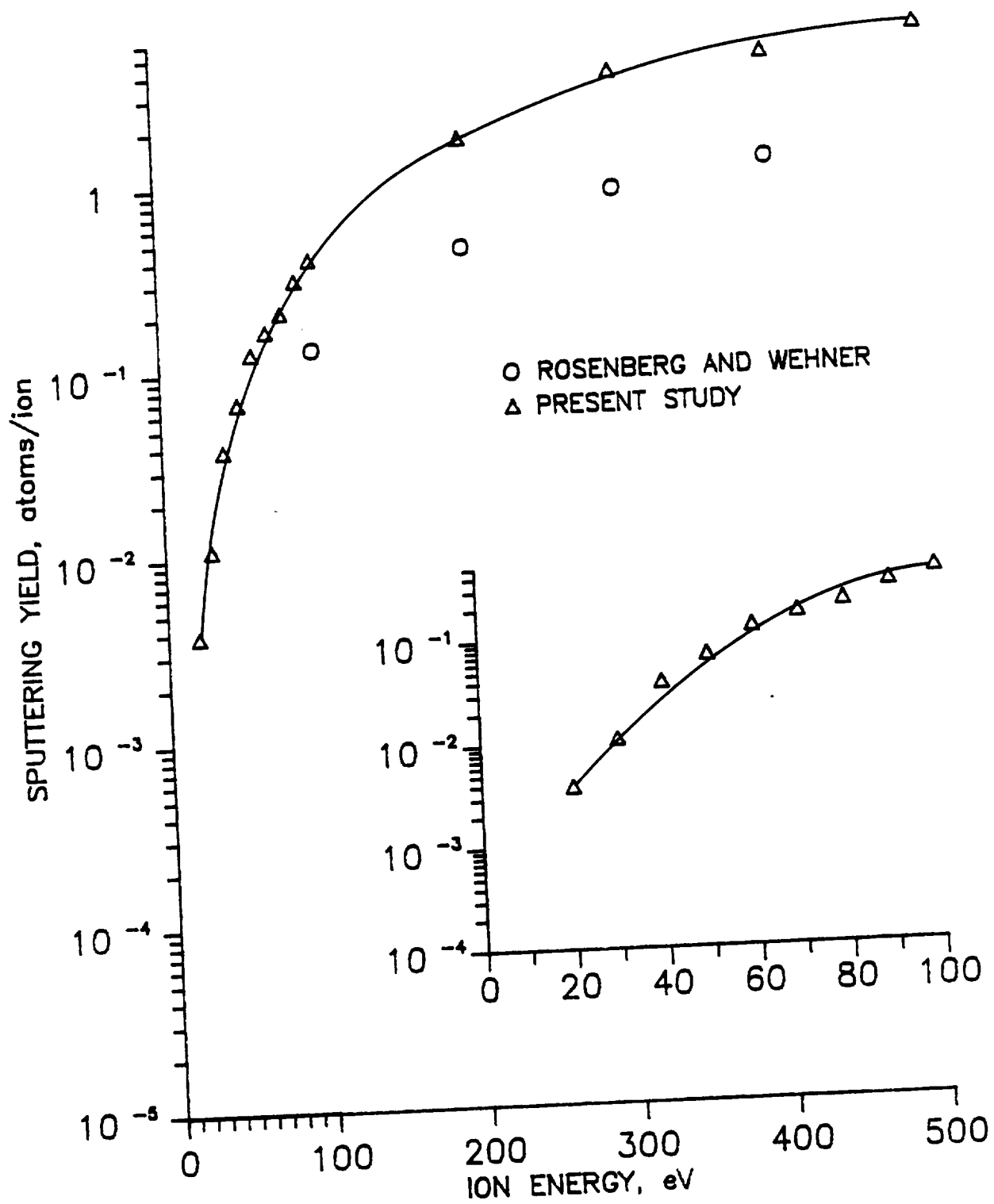


Figure 25. Sputtering Yield of Chromium by Xenon Ions

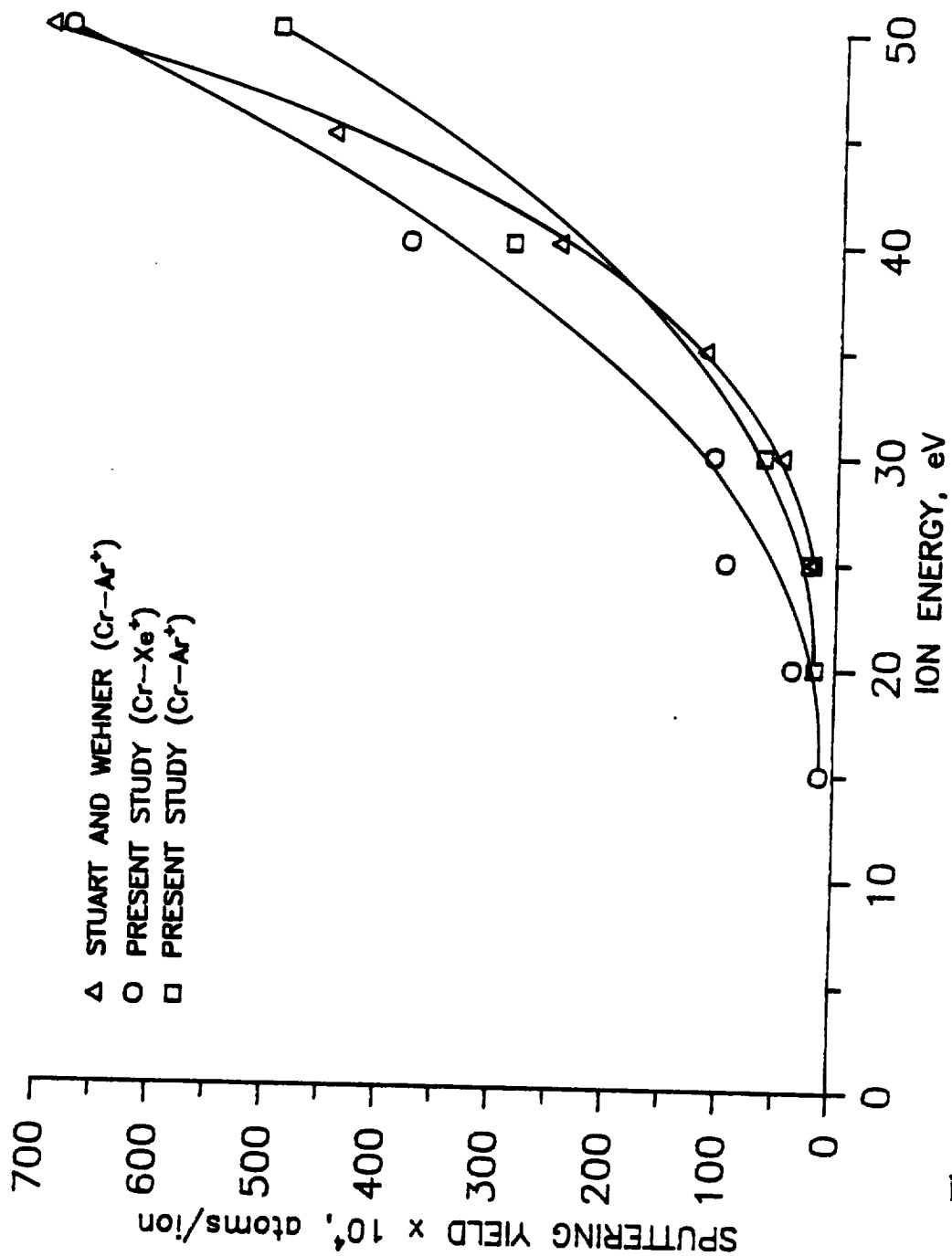


Figure 26. Sputtering Yield of Chromium by Argon and Xenon Ions Near Threshold Energy

^{51}Cr . Hence it is not apparent whether the absence of sputtering was due to a low signal-to-background ratio or whether the threshold of chromium had been reached.

The Cr-Ar^+ yields reported by Wehner are also plotted in Fig. 26 for comparison. Again the concave nature of the yield-energy curve is clearly seen.

Comparative Evaluation of Sputtering Yields

The sputtering yields of cobalt, cadmium and chromium by argon ions obtained from our experiments are plotted in Fig. 27 on a semi-logarithmic scale and in Fig. 28 on a linear scale (10 to 50 eV for cobalt and cadmium and 20 to 30 eV for chromium). The yields by xenon ions are shown in Fig. 29 on a semi-logarithmic scale and in Fig. 30 on a linear scale (10 to 50 eV for cobalt and cadmium and 15 to 25 eV for chromium). It can be seen that chromium has the highest yield and cadmium the lowest. The sputtering yields of cobalt are somewhat higher than those of cadmium (except at 15 and 25 eV Xe^+ energies) but are still considerably lower than those of chromium. The yields of cobalt were found to be as high as 7 times those of cadmium. The yields of chromium, on the other hand, varied from 20 to 100 times those of cadmium.

When these experiments were initiated, we expected to obtain sputtering yields lower than those measured by using a high density plasma discharge. It was assumed that the ions at the low ion current densities obtained from the ion gun would be unable to fully sputter the surfaces by overcoming the continuous formation of adsorbed gas layers. The measured sputtering yields of cobalt and cadmium, especially at higher energies, justify this assumption. However, the yields of chromium were found to be comparable and in many

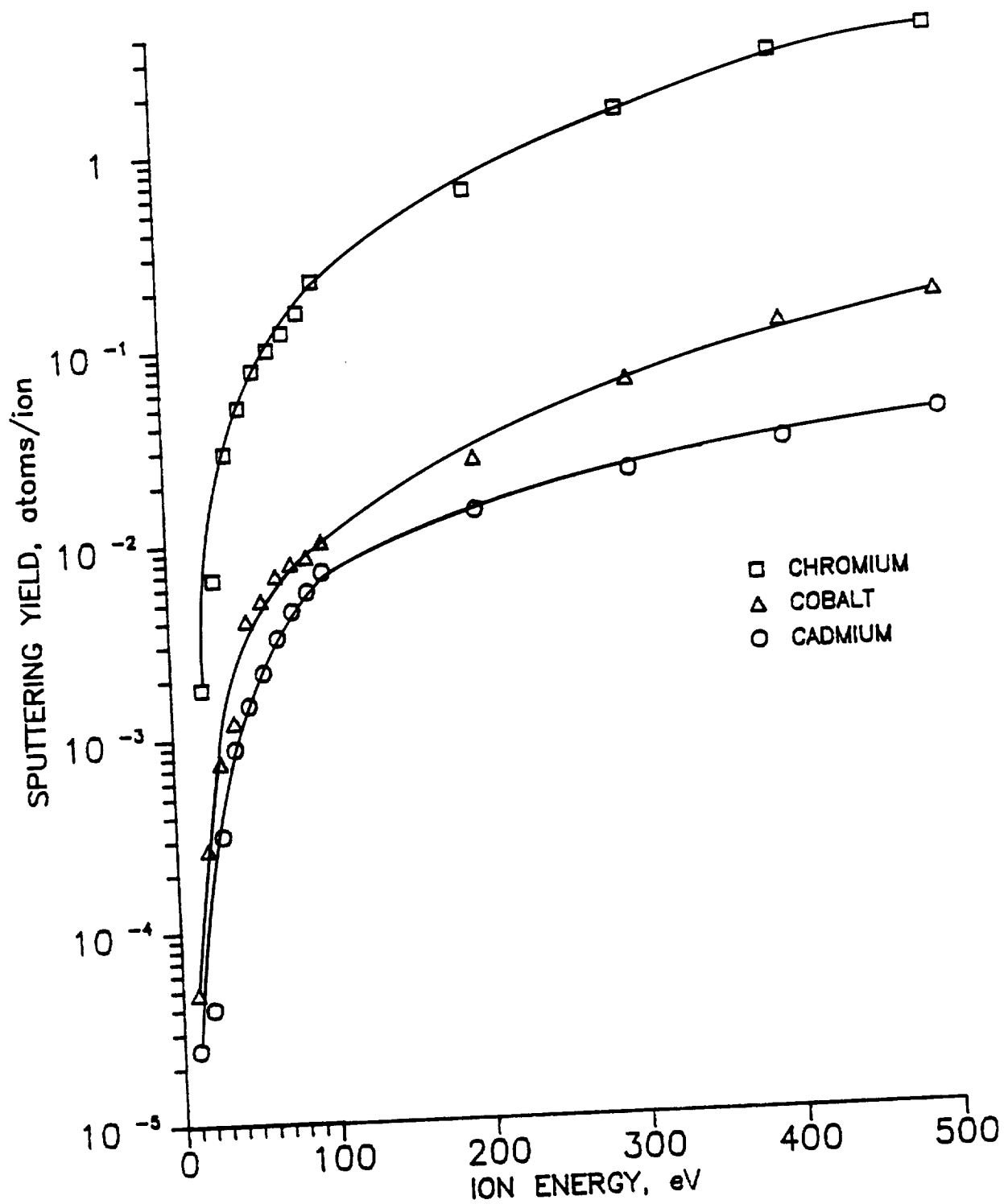


Figure 27. Comparison of the Yields of Cobalt, Cadmium and Chromium by Argon Ions

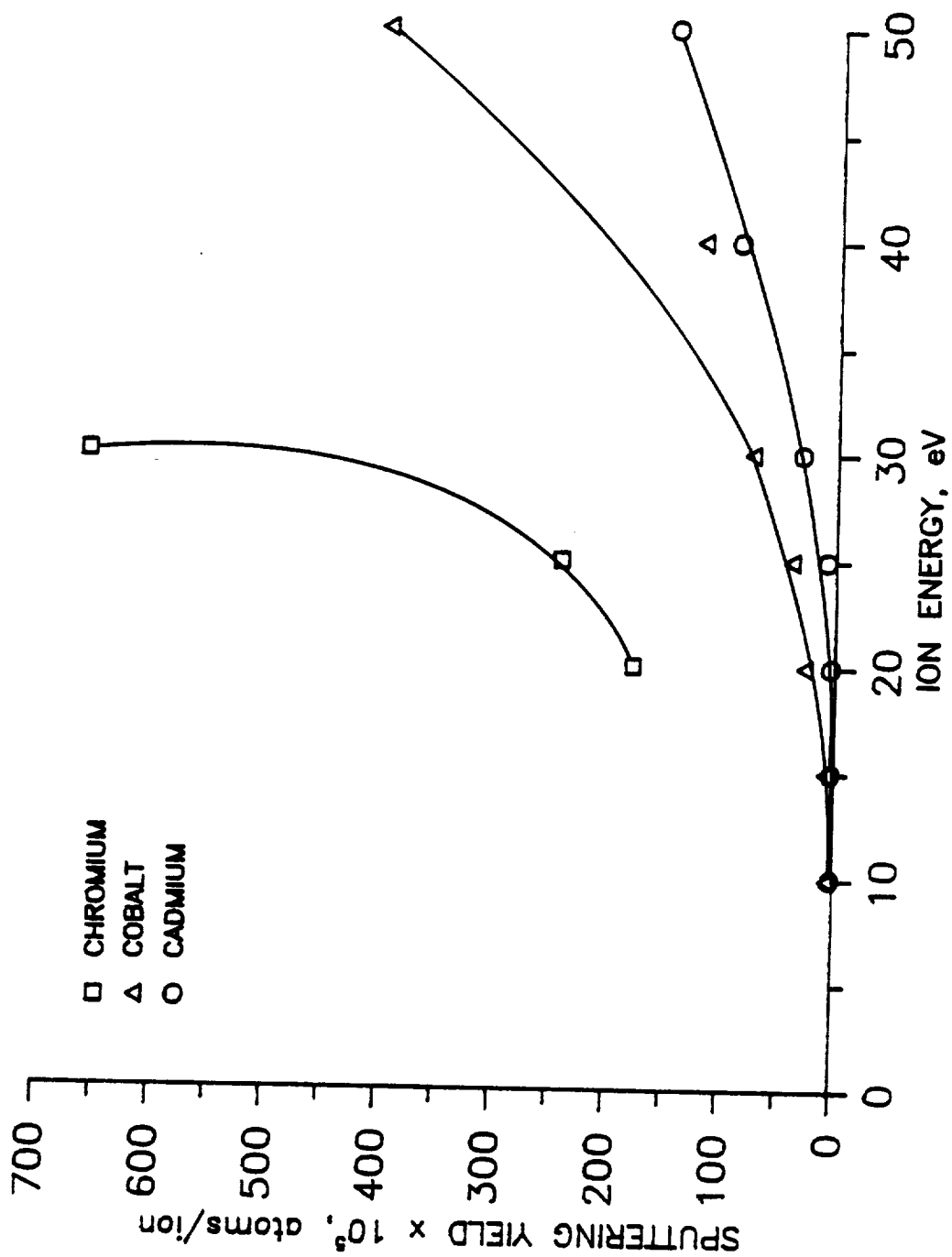


Figure 28. Comparison of the Yields of Cobalt, Cadmium and Chromium by Argon Ions Near Threshold Energy

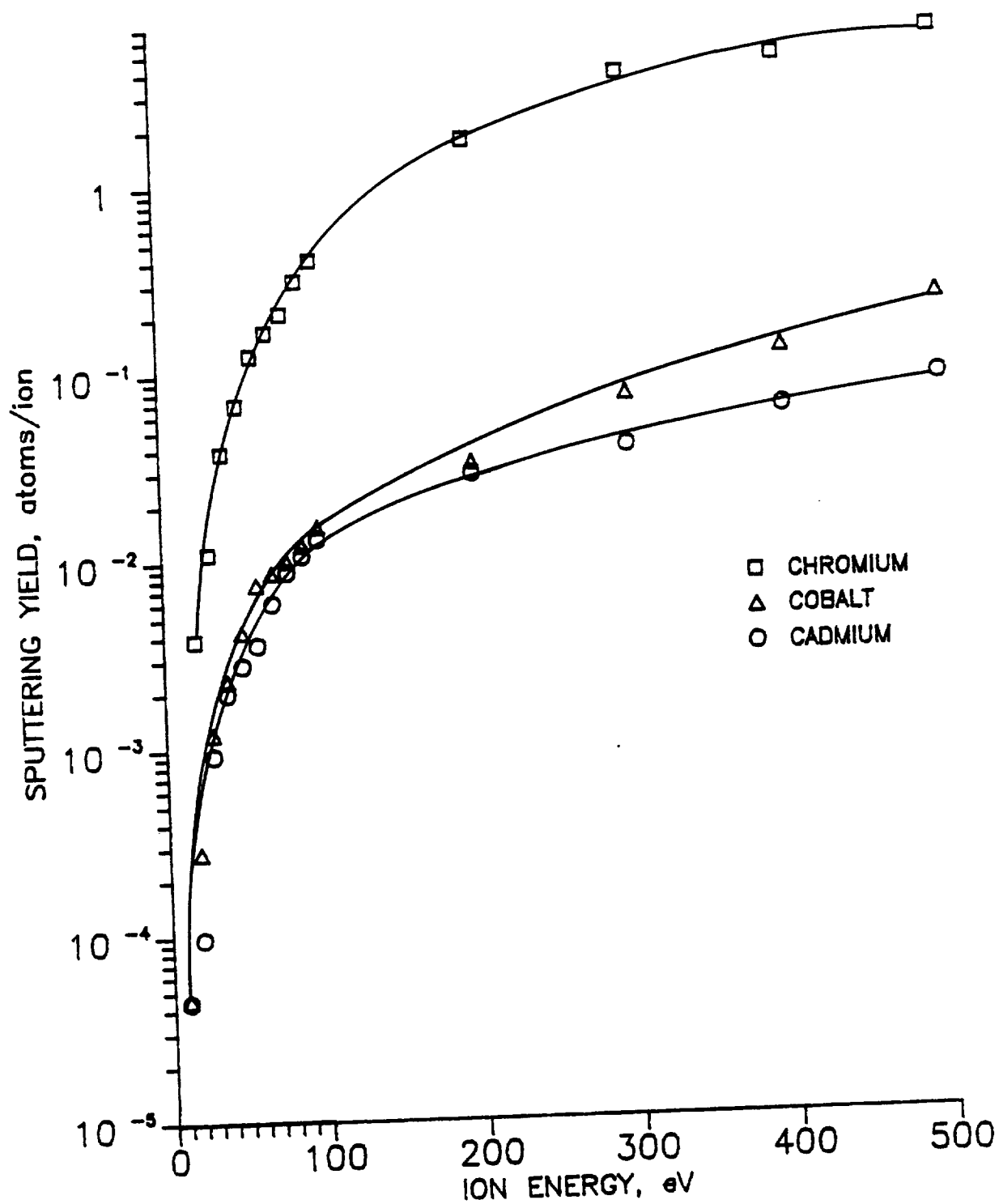


Figure 29. Comparison of the Yields of Cobalt, Cadmium and Chromium by Xenon Ions

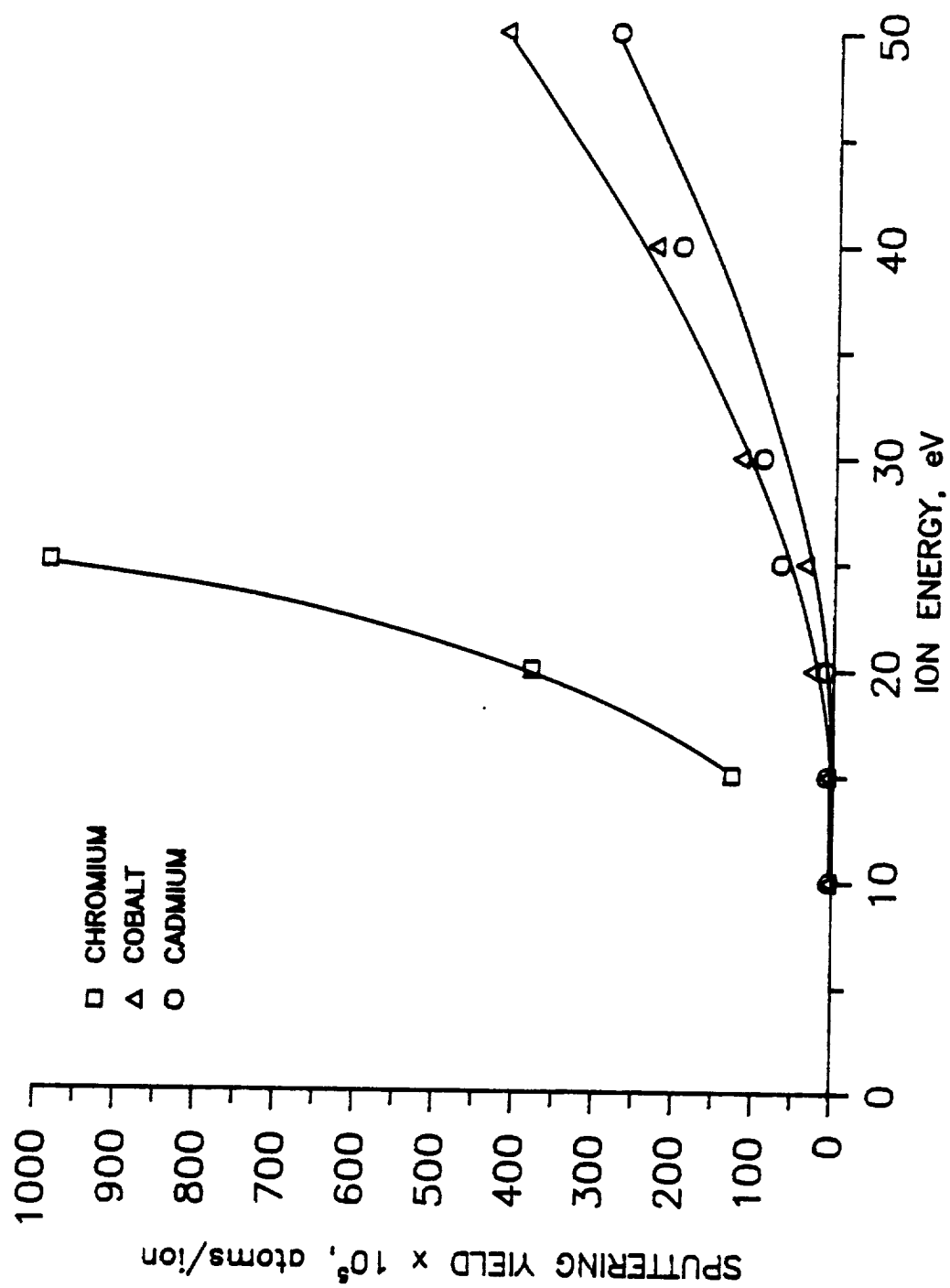


Figure 30. Comparison of the Yields of Cobalt, Cadmium and Chromium by Xenon Ions Near Threshold Energy

instances, higher than those obtained from the plasma-discharge experiments. This came as a surprise and tends to indicate that chemical reactions at the surfaces may be more important in inhibiting the sputtering process than low ion current densities as such.

The concave nature of the yield-energy curve near threshold energy brings the current concept of sputtering threshold into question. Although only three targets were used in this investigation, all yield-energy curves display the concave nature near threshold energies. This trend was first observed by Morgulis and Tischenko [16]. Moreover, when Stuart and Wehner's low-energy yields are plotted on a linear scale, the concave nature of the curves also become evident.

At present, the threshold energy of an element for ion sputtering is considered to be approximately $4H$ where H is the heat of sublimation of the element. For example, a threshold energy of about 16 eV is obtained for cobalt using this formula. Our experiments indicate that the threshold energy for cobalt is lower than 10 eV. However, we could not run our experiments below 10 eV, because in this energy range the ion beam current drops drastically. Morgulis and Tischenko estimated the threshold energy of cobalt by argon and mercury ions to be 7 to 8 eV by linearly extrapolating their yield energy data [16].

MODELING OF DISCHARGE CHAMBER COMPONENT EROSION

Introduction

Ion engines are required to have operational lifetimes of at least 10,000 hours for successful completion of many proposed space missions because these engines operate at low thrust levels. The J-series 30-cm diameter mercury ion engines producing 2 A beam current were developed and extensively tested in the 1970s and early 1980s to accomplish the proposed space propulsion missions which were envisioned at that time. Although mercury was used as the propellant in the development of the ion thrusters, inert gases, especially xenon, is now considered as the favored propellant.

New mission goals, such as primary propulsion for near-Earth and interplanetary missions, require higher thrust produced by each thruster. This can be achieved by increasing the beam current. In the long endurance tests of the J-series mercury ion thrusters, various discharge chamber components have revealed substantial erosion induced by ions. Since xenon ions have higher sputtering yields compared to mercury ions with same energy, it is expected that xenon ion thruster components will erode at a higher rate compared to those of mercury ion thrusters. This fact coupled with the requirement of higher discharge current (to produce higher beam current) imply that xenon ion engine

operating life will be severely limited by ion sputter erosion of discharge chamber components.

The most severe erosion is expected from the discharge chamber components which are at or near the cathode potential. These include the screen grid, the cathode keeper and in the J-series thruster, the baffle and the cathode pole piece assembly. The maximum erosion is always observed on the upstream side of the baffle in the J-series thrusters. Discharge chambers using a ring cusp magnetic field and having no baffles are presently being extensively investigated as an alternative to the J-series thrusters [5].

Physical Sputtering

A. Mathematical Model : The ions inside the discharge chamber are at the potential of the plasma in which they are produced. They acquire a kinetic energy equal to the plasma-to-cathode potential difference as they fall through a sheath and strike the surfaces at or near the cathode potential. Both singly and doubly charged ions have been observed inside the discharge chamber. The ratio of the two species of ions at a given location is determined by the discharge voltage as well as the nature and the mass flow rate of the propellant. Let j^+ and j^{++} be the current densities of the singly and doubly charged ions respectively at a given location. For simplicity, it is assumed here that all singly charged ions in the same region have equal energy and

all doubly charged ions in that region have twice the energy of singly charged ions. The number of singly charged ions, n^+ , striking the unit area of a surface per unit time is

$$n^+ = \frac{j^+}{q} \quad (15)$$

where q is the charge of an electron. The number of doubly charged ions, n^{++} , striking the unit area of the surface per unit time is

$$n^{++} = \frac{j^{++}}{2q} \quad (16)$$

The surface atom removal rate by sputtering per unit area, N_t , is then given by

$$\begin{aligned} N_t &= n^+ S(E) + n^{++} S(2E) \\ &= \frac{1}{q} \left\{ j^+ S(E) + \frac{j^{++} S(2E)}{2} \right\} \end{aligned} \quad (17)$$

where S is the sputtering yield and E and $2E$ are the energies of the singly and doubly charged ions respectively. If N_v is the number density of atoms, then the wear rate, w is given by

$$w = \frac{j^+}{q N_v} \left\{ S(E) + \frac{j^{++} S(2E)}{2j^+} \right\} \quad (18)$$

The number density of atoms can be expressed as

$$N_v = \frac{\rho A}{M} \quad (19)$$

where ρ is the density, A is the Avogadro's number and M is the atomic weight of the material. Denoting the total current density j by

$$j = j^+ + j^{++} \quad (20)$$

and

$$\beta = \frac{j^{++}}{j^+} \quad (21)$$

j^+ can be written as

$$j^+ = \frac{j}{1 + \beta} \quad (22)$$

Using Eq. 20 and Eq. 22, the wear rate can be given by

$$w = \frac{jM}{2(1 + \beta)q\rho A} \{2S(E) + \beta S(2E)\} \quad (23)$$

B. Screen Grid Centerline Erosion : The screen grid is considered the principal life-limiting component of the ion thrusters. It is exposed to a high flux of energetic ions, yet it must be thin for good performance of the thruster [26]. Quantitative results from several long endurance tests with mercury propellants at approximately 2 A beam current indicate that the screen grid centerline erosion rates are in the range of 5 to 35 nm/hr.

The screen grid is made of molybdenum. In a discharge chamber operating at 32 V, it is exposed to ions having energies of about 32 eV (for singly charged ions) and 64 eV (for doubly charged ions). The sputtering yield of molybdenum by mercury ions at 64 eV is about 2.3×10^{-3} and the extrapolated sputtering yield at 32 eV is about 2×10^{-4} [22]. The ratio of doubly to singly charged ions is dependent on the discharge voltage and generally varies from 0.15 to 0.3. The ion flux impinging on the screen electrode, j_s , is related to the beam current, J_b , by

$$j_s = \frac{J_b}{A_b F \phi_s} \quad (24)$$

where A_b is the beam area, F is the beam flatness parameter and ϕ_s is the effective transparency of the screen electrode defined by [27]

$$\phi_s = \frac{J_b}{J_b + J_s} \quad (25)$$

J_s is the screen electrode current. For a 30-cm diameter mercury ion thruster, $A_b = 573 \text{ cm}^2$, $F = 0.5$ and ϕ_s is approximately equal to 0.85 [27]. Using these values in Eq. 23, the erosion rate of the screen grid centerline can be calculated as a function of β . The calculated erosion rate is shown in Fig. 31. It is observed that for $\beta = 0.15$ the erosion rate is 9.32 nm/hr whereas for $\beta = 0.3$ the erosion rate is 12.07 nm/hr. These erosion rates compare well with the erosion rate of 6.4 nm/hr obtained from the mission profile life test (MPLT) [11]. It can also be seen from Fig. 31 that the erosion rate is not highly sensitive to the value of β .

When the voltage in the discharge chamber is increased, the ions impinge on the cathode potential surfaces at higher energies. For a discharge chamber operating at 36 V, the energies of the ions will be 36 and 72 eV respectively for singly and doubly charged ions. The corresponding sputtering yield values are 3×10^{-4} and 5×10^{-3} [22]. The centerline erosion rate at 36 V and at $\beta = 0.3$ is 23.2 nm/hr which is comparable to the erosion rates of 31 to 35 nm/hr measured from several long duration endurance tests at 36 V [9,28,29]. Hence it is concluded that the screen grid centerline erosion rates of J-series mercury ion thrusters can be estimated reasonably well given the uncertainty in the

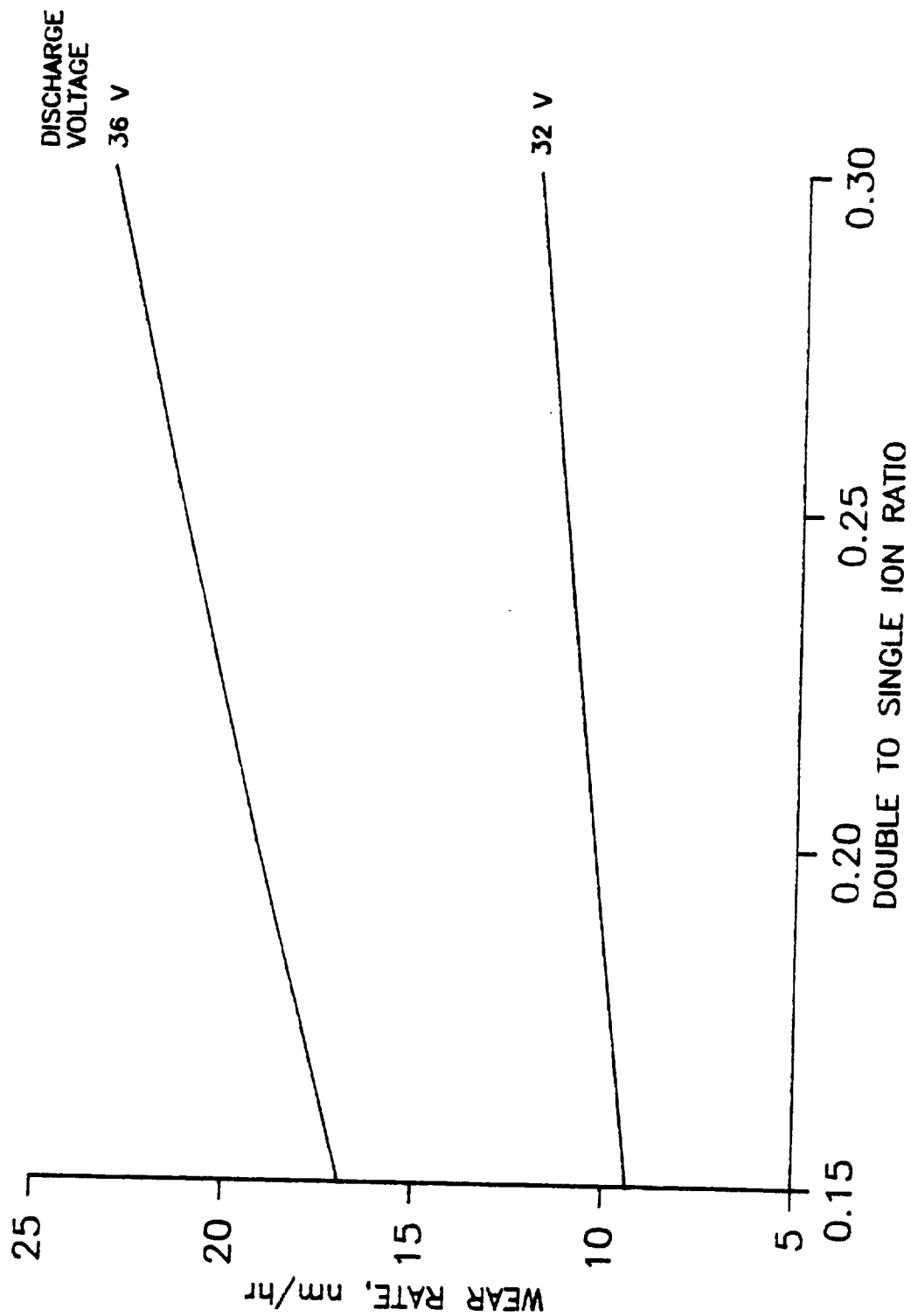


Figure 31. Variation of Screen Grid Centerline Erosion with Ratio of Doubly to Singly Charged Ions

sputtering yield data at low energies.

Erosion rates at screen grid centerline has also been measured in modified J-series ion thrusters using xenon. An erosion rate of 25.5 nm/hr was obtained in one test at a discharge voltage of 32 V and 2 A beam current [30]. In another test with a 28 V discharge and 5 A beam current the erosion rate was observed to be 9 nm/hr which could go as high as 27 nm/hr when facility effects are taken into account [12]. Since xenon ions have higher sputtering yields compared to mercury ions with same energy, the increased erosion rates observed in the xenon ion thrusters can be qualitatively justified. However no quantitative comparison could be made because Mo-Xe⁺ sputtering yields at low energies are not available.

C. Baffle Erosion : A metallic disc (baffle) is placed downstream of the hollow cathode in the J-series ion thrusters to improve the ionization efficiency. During the endurance tests it was observed that the upstream side of the baffle eroded at a high rate. For example, the upstream side of the tantalum baffle was found to wear at 10 nm/hr during the MPLT [11]. Although no measurement of plasma potential in this region has been made because of the very hostile environment, it is generally assumed to be at approximately the keeper voltage which is about 10 V. Also, on the basis of theoretical calculations it is assumed that there are no doubly charged ions in this region [14]. Since the generally accepted thresholds for sputtering were well beyond 10 eV,

the origin and the energy of the ions causing the upstream baffle erosion was a mystery. In light of the data obtained in our experiments, this erosion can at least be qualitatively explained as caused by the ions within the confines of the cathode pole piece plasma having a potential of about 10 V.

It is not possible at this time to calculate the erosion rate of the upstream baffle using Eq. 23 because the value of the ion current density in this region is not known. A recent study on a laboratory model ring cusp discharge chamber has revealed the presence of ions near the cathode having energies as high as 50 eV at discharge currents exceeding 10 A [15]. If the presence of these higher energy ions (called jet ions) are confirmed in future investigations of J-series mercury or xenon ion thrusters, the discharge chamber component erosion can be attributed to both low-energy and jet ions.

CONCLUSIONS

Cobalt and cadmium targets were observed to sputter at energies as low as 10 eV for both argon and xenon ions. The chromium yields could not be measured below 20 eV for argon ions and 15 eV for xenon ions. The sputtering yields of cobalt and cadmium by argon and xenon ions were found to be considerably lower than those measured in experiments using high-density plasma discharges, especially at high ion energies. This was expected since the ion guns produce ion current densities which are orders of magnitude lower than those obtainable from experiments using plasma discharges. However, at low ion energies, the sputtering yields obtained from our experiments become comparable to those obtained from high-density plasma discharge experiments. The reason for this is not clear.

The yields of chromium by both argon and xenon ions were found to be comparable and in many cases, higher than those obtained from the plasma discharge experiments. This surprising result tends to indicate that chemical reactions at the surfaces may be playing a more important role in inhibiting the sputtering process than low ion current densities as such.

The yield-energy curves near threshold energies become concave when plotted on a linear scale, deviating from the

expected straight line form. In light of this information, the theoretical model for low-energy sputtering and especially, the concept of a sputtering threshold need to be reexamined.

The existence of sputtering at ion energies as low as 10 eV qualitatively explain the erosion observed in the discharge chambers of the J-series mercury ion thrusters. The calculated centerline screen grid erosion rates compare favorably with those measured from the long duration thruster tests. However, the upstream baffle erosion rate could not yet be quantified as the nature of the plasma within the confines of the cathode pole piece is not fully known.

REFERENCES

1. SPONABLE, J.M. and PENN, J.P., "An Electric Orbit Transfer Vehicle for Delivery of NAVSTAR Satellites", AIAA Paper 87-0985 (1987).
2. SCHREIB, R., "Utility of Xenon Ion Stationkeeping," AIAA Paper 86-1849 (1986).
3. CAVENY, L. and VONDRA, R., "Ion Propulsion Goals for Earth Orbit Transfers," AIAA Paper 90-2621 (1990).
4. SMITH, P., "Maximizing the Near-Term Benefits of Ion Propulsion on Geostationary Spacecraft," AIAA Paper 90-2623 (1990).
5. BEATTIE, J.R. and MATOSSIAN J.N., "Mercury Ion Thruster Technology," NASA CR 174974 (1989).
6. BROPHY, J.R., "Ion Thruster Performance Model," NASA CR-174810 (1984).
7. BASSNER, H., BERG, H. and KUKES, R., "The Design of RITA Electric Propulsion System for Sat 2," AIAA Paper 90-2539 (1990).
8. GROH, K., LOEB, H., FELL, J., WEBER, F. and ZARNITZ, F., "Development Status of the RIT-Ion Engines," AIAA Paper 90-2671 (1990).
9. COLLETT, C.R. and POESCHEL, R.L., "A 10,000 Hour Endurance Test of a 700 Series 30-cm Engineering Model Thruster," AIAA Paper 76-1019 (1976).
10. NAKANISHI, S. and FINKE, R.C., "9700-Hour Durability Test of a Five Centimeter Diameter Ion Thruster," J. Spacecraft and Rockets, 11, 560 (1974)

11. BECHTEL, R.T., TRUMP, G.E. and JAMES, E.J., "Results of the Mission Profile Life Test," AIAA Paper 82-1905 (1982).
12. RAWLIN, V.K., "Internal Erosion Rates of a 10-kW Xenon Ion Thruster," AIAA paper 88-2192 (1988).
13. BROPHY, J.R. and GARNER, C.R., "Tests of High Current Hollow Cathodes for Ion Engines," AIAA Paper 88-2913 (1988).
14. COLLETT, C.R., "Thruster Endurance Test," NASA CR 135011 (1976).
15. FRIEDLY, V.J., "Hollow Cathode Operation at High Discharge Currents," NASA CR-185238 (1990).
16. MORGULIS, N.D. and TISCHENKO, V.D., "The Investigation of Cathode Sputtering in the Near Threshold Region," Soviet Phys.-JETP 3, 52 (1956).
17. WEHNER, G.K., "Sputtering Yields for Normally Incident Hg^+ -Ion Bombardment at Low Ion Energy," Phys. Rev. 108, 35 (1957).
18. LAEGREID, N. and WEHNER, G.K., "Sputtering Yields of Metals for Ar^+ and Ne^+ Ions with Energies from 50 to 600 eV," J. Appl. Phys. 32, 365 (1961).
19. ROSENBERG, D. and WEHNER, G.K., "Sputtering Yields for Low Energy He^+ -, Kr^+ -, and Xe^+ - Ion Bombardment," J. Appl. Phys. 33, 1842 (1962).
20. STUART, R.V. and WEHNER, G.K., "Sputtering Yields at Very Low Bombarding Ion Energies," J. Appl. Phys. 33, 2345 (1962).
21. WEHNER, G.K. and ANDERSON, G.S., in Handbook of Thin Film Technology, Ed. L.I. Maissel and G. Reinhard, McGraw-Hill, New York (1970). Pg. 3-18.

22. ASKEROV, Sh.G. and SENA, L.A., "Cathode Sputtering of Metals by Slow Mercury Ions," Soviet Phys. Solid State 11, 1288 (1969).
23. TOMPKINS, H.G., An Introduction to the Fundamentals of Vacuum Technology, AVS Monograph series, Ed. N.R. Whetten, American Institute of Physics, New York (1984). Pg. 8.
24. WEHNER, G.K., "Controlled Sputtering of Metals by Low-Energy Hg Ions," Phys. Rev. 102, 690 (1956).
25. STUART, R.V. and WEHNER, G.K., "Sputtering Thresholds and Displacement Energies," Phys. Rev. Letters 4, 409 (1960).
26. BEATTIE, J.R., "Endurance Test of a 30-cm-Diameter Engineering Model Ion Thruster," NASA CR-168132 (1983).
27. BEATTIE, J.R., "A Model for Predicting the Wearout Lifetime of the LeRC/HUGHES 30-cm Mercury Ion Thruster," AIAA Paper 79-2079 (1979).
28. COLLETT, C.R. and BECHTEL, R.T., "An Endurance Test of a 900 Series 30-cm Engineering Model Ion Thruster," AIAA Paper 81-0716 (1981).
29. COLLETT, C.R., "Endurance Test of a 30-cm Diameter Engineering Model Ion Thruster," Monthly Contractor Report No. 34 and 35, Hughes Research Laboratories (1977).
30. GARNER, C.E., BROPHY, J.R., PLESS, L.C. and BARNETT, J.W., "The Effect of Nitrogen on Xenon Ion Engine Erosion," AIAA Paper 90-2591 (1990).

APPENDIX A
SPUTTERING YIELD DATA

Table A.1 Sputtering Yield Data of Cobalt

Ion Energy (eV)	Incident Ion Species		
	Cesium	Argon	Xenon
500	0.19	0.15	0.22
400	0.14	0.113	0.12
300	7.7×10^{-2}	0.06	7.1×10^{-2}
200	2.3×10^{-2}	2.5×10^{-2}	3.2×10^{-2}
100	2.03×10^{-3}	1.0×10^{-2}	1.5×10^{-2}
90		8.4×10^{-3}	1.2×10^{-2}
80		7.8×10^{-3}	9.92×10^{-3}
75		7.4×10^{-3}	9.3×10^{-3}
70		6.8×10^{-3}	8.6×10^{-3}
60		5.08×10^{-3}	7.5×10^{-3}
50		4.0×10^{-3}	4.2×10^{-3}
40		1.2×10^{-3}	2.3×10^{-3}
30		7.5×10^{-4}	1.2×10^{-3}
25		3.9×10^{-4}	3.81×10^{-4}
20		2.68×10^{-4}	2.8×10^{-4}
15		7.58×10^{-5}	7.11×10^{-5}
10		4.8×10^{-5}	4.5×10^{-5}

Table A.2 Sputtering Yield Data of Cadmium

Ion Energy (eV)	Incident Ion Species	
	Argon	Xenon
500	3.72×10^{-2}	8.19×10^{-2}
400	2.8×10^{-2}	5.88×10^{-2}
300	2.07×10^{-2}	3.8×10^{-2}
200	1.37×10^{-2}	2.8×10^{-2}
100	7.02×10^{-3}	1.3×10^{-2}
90	5.58×10^{-3}	1.06×10^{-2}
80	4.44×10^{-3}	8.68×10^{-3}
75		6.01×10^{-3}
70	3.22×10^{-3}	5.94×10^{-3}
60	2.14×10^{-3}	3.58×10^{-3}
50	1.46×10^{-3}	2.78×10^{-3}
40	8.82×10^{-4}	1.97×10^{-3}
30	3.16×10^{-4}	9.21×10^{-4}
25	8.14×10^{-5}	6.85×10^{-4}
20	3.98×10^{-5}	9.65×10^{-5}
15	3.18×10^{-5}	7.90×10^{-5}
10	2.45×10^{-5}	4.38×10^{-5}

Table A.3 Sputtering Yield Data of Chromium

Ion Energy (eV)	Incident Ion Species	
	Argon	Xenon
500	3.48	5.77
400	2.74	4.34
300	1.47	3.62
200	0.60	1.67
100	0.218	0.402
90	0.152	0.310
80	0.12	0.207
70	9.87×10^{-2}	0.165
60	7.74×10^{-2}	0.125
50	4.99×10^{-2}	6.82×10^{-2}
40	2.9×10^{-2}	3.81×10^{-2}
30	6.57×10^{-3}	1.10×10^{-2}
25	2.42×10^{-3}	9.85×10^{-3}
20	1.78×10^{-3}	3.80×10^{-3}
15		1.27×10^{-3}

DISTRIBUTION LIST

	<u>Copies</u>
National Aeronautics and Space Administration Washington, DC 20546 Attn:	
RP/Mr. Earl E. VanLaningham, MS B600	1
RP/Mr. Gary Bennett, MS B600	1
RP/Mr. Marcus Watkins, MS B600	1
National Aeronautics and Space Administration Marshall Space Flight Center Huntsville, AL 35812 Attn:	
Mr. Robert Bechtel, EB 11	5
Procurement Office, AP 29E	2
Dr. George Fichtl, ES 01	1
Dr. Joseph Randall, EB 01	1
Mr. James Rice, CE 01	1
Mr. Ralph Carruth, ES 53	1
Mr. Jason Vaughn, ES 53	1
National Aeronautics and Space Administration Lewis Research Center 21000 Brookpark Road Cleveland, OH 44135 Attn:	
Mr. Dave Byers, MS 500-219	1
Mr. Jim Sovey, MS 500-219	1
Mr. Vincent Rawlin, MS 500-219	1
Mr. Bruce Banks, MS 302-1	1
Dr. Frank Curran, MS 500-219	1

National Aeronautics and Space Administration
Lyndon B. Johnson Space Center
Houston, TX 77058

Attn:

Dr. James E. McCoy, Mail Code SN3

1

Air Force Astronautics Lab
Edwards AFB, CA 93523

Attn:

LSVE/Mr. J. Chris Andrews

1

LKDH/Lt. Phil Roberts, MS 24

1

Jet Propulsion Laboratory
4800 Oak Grove Laboratory
Pasadena, CA 91109

Attn:

Mr. James Graf

1

Dr. John Brophy, MS 125-224

1

Dr. Charles Garner, MS 125-224

1

Hughes Research Laboratories
3011 Malibu Canyon Road
Malibu, CA 90265

Attn:

Dr. Jay Hyman, MS RL 57

1

Dr. J.R. Beattie, MS RL 57

1

Dr. J.N. Matossian, MS RL 57

1

Engineering Quadrangle
Princeton University
Princeton, NJ 08540

Attn:

Prof. R.G. Jahn

1

Dr. Arnold Kelly

1

Ion Tech Inc.
2330 E. Prospect Road
Fort Collins, CO 80525
Attn:

Dr. Gerald C. Isaacson	1
Dr. Dan Siegfried	1
Mr. Larry Daniels	1

Colorado State University
Fort Collins, CO 80521
Attn:

Prof. P.J. Wilbur	1
Prof. H.R. Kaufman	1

Dr. Robert Vondra	1
-------------------	---

P.O. Box 596
Wrightwood, CA 92397

Electric Propulsion Laboratory, Inc.
43423 N. Division St., Suite 205
Lancaster, CA 93535
Attn:

Dr. Graeme Aston	1
------------------	---

University of Tennessee Space Institute
Tullahoma, TN 37388-8897
Attn:

Mr. Verlin Friedly	1
--------------------	---

Center for Aerospace Research

Case Western Reserve University
10900 Euclid Avenue
Cleveland, OH 44106
Attn:

Dr. Eli Reshotko	1
------------------	---

Intelsat

3400 International Dr. N.W.

Washington D.C. 20008-3098

Attn:

Mr. Bernard Free, MS 33

1

TRW Inc.

TRW Systems

One Space Park

Redondo Beach, CA 90278

Attn:

Mr. Sid Zafran

1

Boeing Aerospace Co.

P.O. Box 3999

Seattle, WA 98124-2499

Attn:

Dr. J.S. Meserole, MS 82/83

1

Lockheed Missiles and Space Co.

Sunnyvale, CA 94088

Attn:

Dr. William L. Owens, Dept. 57-24

1

Rocket Research Co.

P.O. Box 97009

Redmond, WA 98073-9709

Attn:

Mr. William W. Smith

1

Mr. Paul Lichon

1

Dr. Dave King

1

Sandia Laboratories

P.O. Box 5800

Albuquerque, NM 87185

Attn:

Mr. Ralph R. Peters, Mail Code 4537

1

Mr. Dean Rovang, Mail Code 1251

1

EG & G Idaho
P.O. Box 1625
Idaho Falls, ID 83401
Attn:

Dr. G.R. Longhurst, TSA-104 1

Michigan State University
East Lansing, MI 48824
Attn:

Dr. J. Asmussen 1

Dr. M.C. Hawley 1

Physics Department
Naval Postgraduate School
Monterey, CA 93943-5000
Attn:

Dr. Chris Olson, Mail Code 61-0S 1

Martin Marietta Aerospace
P.O. Box 1620
LaJolla, CA 92038
Attn:

Dr. Ira Katz 1

Dept. of Aero. & Astro. Engineering
101 Transportation Bldg.
104 South Mathews Ave.
Urbana, IL 61801-2997
Attn:

Dr. Rodney Burton 1

